

# Partitioning of cloud water and rainwater content by ground-based observations with the Advanced Microwave Radiometer for Rain Identification (ADMIRARI) in synergy with a micro rain radar

Pablo Saavedra,<sup>1</sup> Alessandro Battaglia,<sup>2</sup> and Clemens Simmer<sup>1</sup>

Received 19 July 2011; revised 28 December 2011; accepted 29 December 2011; published 3 March 2012.

[1] Cloud and rain liquid water path and total water vapor are retrieved simultaneously from passive microwave observations with the multifrequency dual-polarized Advanced Microwave Radiometer for Rain Identification (ADMIRARI). A data set of linearly polarized brightness temperatures has been collected at 30° elevation angle together with slant radar reflectivity profiles at 24.1 GHz from a micro rain radar (MRR) pointing into the same viewing direction. The slant path integrated values are retrieved via a Bayesian inversion approach, the quality of which is evaluated by a simulation-based retrieval sensitivity study. The algorithm includes a physical constraint by taking into account the rain column structural information from the MRR observations. Measurements and derived path-integrated water component estimates from 23 August to 12 November 2008, obtained in Cabauw, Netherlands, are analyzed. During raining cloud conditions the zenith-normalized root-mean-square error for water vapor, cloud liquid water path, and rain liquid water path are, on average, estimated to 1.54 kg m<sup>-2</sup>, 144 g m<sup>-2</sup>, and 52 g m<sup>-2</sup>, respectively. On the basis of these results, long-term estimated distributions of cloud water–rainwater partitioning for midlatitude precipitating clouds are presented for the first time as obtained by a ground-based radiometer.

**Citation:** Saavedra, P., A. Battaglia, and C. Simmer (2012), Partitioning of cloud water and rainwater content by ground-based observations with the Advanced Microwave Radiometer for Rain Identification (ADMIRARI) in synergy with a micro rain radar, *J. Geophys. Res.*, 117, D05203, doi:10.1029/2011JD016579.

## 1. Introduction

[2] Liquid water clouds play an important role in Earth's climate through the reflection, absorption and emission of radiation. They reduce the incoming solar radiation because of their relatively high albedo, governing the downward long-wave radiation with a strong dependence on water vapor distribution and the effective cloud base height. In order to better quantify those effects, more accurate information about the cloud water content is needed, being this parameter the most critical driver for radiative effects [Salby, 1996, pp. 306–308; Stephens and Webster, 1984; Crewell et al., 2004]. Cloud liquid water content is also a prognostic variable in Numerical Weather Prediction and Climate models, therefore reliable observations are required for validation and improvement of these models.

[3] Direct estimates of cloud liquid water content are only available from costly aircraft in situ measurements confining their availability to short periods and special locations. Remote sensing by ground-based microwave radiometers is

increasingly used to probe the cloudy atmosphere often in synergy with other observations, to retrieve the vertically integrated cloud liquid water path (hereafter CLWP) [e.g., Crewell et al., 2001; Loehnert and Crewell, 2003; Crewell and Loehnert, 2003; Crewell et al., 2004; Rose et al., 2005]. Estimates of profiles of temperature, water vapor and even cloud liquid water are possible with temporal resolutions of 1–5 min and ranges up to 10 km [e.g., Knupp et al., 2009; Crewell et al., 2001]. Recent work by Crewell et al. [2009] concludes, however, that passive microwave profiling of cloud liquid water without additional information from active instruments is only meaningful for very limited situations and large liquid water contents.

[4] Precipitation is one of the most important components of the hydrological cycle and connects it to the heat energy cycle [Marzano et al., 1999; Salby, 1996, pp. 310–311]. Numerous passive and active remote sensing methods have been developed for the quantification of precipitation. Rain rates are typically derived from backscattered signals emitted by ground and spaceborne radars.

[5] The increasing use of ground-based multifrequency passive microwave radiometers for the observation of atmospheric parameters has fostered also their exploitation for retrieving rainfall rates. Water on the usually exposed receiving antenna, however, is a major problem because absorption losses and hardly predictable signals. Moreover,

<sup>1</sup>Meteorological Institute, University of Bonn, Bonn, Germany.

<sup>2</sup>Department of Physics and Astronomy, University of Leicester, Leicester, UK.

the presence of rainwater within the sensed atmospheric volume challenges the applicability of the Rayleigh approximation (emission proportional to liquid water amount) rendering the signal interpretation even more difficult: a liquid water path (LWP) with a significant rain component produces much higher brightness temperatures (TB) than a pure cloud water component and affects the LWP retrieval by a strong increase in RMS and bias errors which can easily exceed  $0.1 \text{ kg m}^{-2}$  even for LWP values below  $1 \text{ kg m}^{-2}$  [e.g., *Loehnert and Crewell*, 2003]. Hardware precaution partially avoid antenna wetting, e.g., by hydrophobic radome coatings, styrofoam windows, blowers or water-repellent films in conjunction with rain covers for shielding during low elevation angle observations [see *Crewell et al.*, 2001; *Marzano et al.*, 2005b; *Maetzler and Morland*, 2008; *Loehnert et al.*, 2011; *Battaglia et al.*, 2009a].

[6] Few studies have been performed in order to estimate cloud and rain LWP simultaneously, i.e., the partition of the total LWP in its cloud and rain components. This partitioning plays an important role in cloud modeling and in space-based retrieval algorithms where empirical assumptions are employed in order to resolve the unknown cloud-rain partition [*Wentz and Spencer*, 1998; *Hilburn and Wentz*, 2008]. The work by *O'Dell et al.* [2008] identifies assumptions related to the partitioning of cloud water and rainwater as a major source of systematic errors in retrievals based on spaceborne instruments. They conclude that the usefulness of microwave-based retrievals of cloud water and rainwater (and derived climatologies) can be severely hampered by these uncertainties. Recently, *Bennartz et al.* [2010] exploited the combined use of passive microwave radiometer and visible–near-infrared observations (AMSR-E and SEVIRI spaceborne instruments) for the detection of precipitation and the derivation of rainwater path in warm clouds utilizing the different physical information content of the two observation types. They found a correlation of  $R^2 = 0.5$  between rainwater path and in-cloud liquid water path, with a strongest correlation of  $R^2 = 0.69$  found between rainwater path and the inverse of cloud droplet number concentration. *Lebsock et al.* [2011] made studies on detecting the ratio of rain and cloud water in low-latitude shallow marine clouds by utilizing satellite observations using the collocated CloudSat profiling radar and the Moderate Resolution Imaging Spectroradiometer (MODIS), the method makes a key assumption that the MODIS is unaffected by the presence of precipitation. Finding a precipitation-to-cloud ratio, increasing from approximately zero at low cloud water path to roughly 0.5 at  $500 \text{ g m}^{-2}$  of cloud water. An interesting feature shown in this work is the occurrence of nonzero rainwater path at very low values of cloud water.

[7] *Matrosov* [2009a] presented an active remote sensing approach to cloud liquid water path and mean rain rate for stratiform precipitation. His method is based on the attenuation by the liquid hydrometeor layer in returns from vertically pointing cloud radars at Ka and W band. The method further requires auxiliary data from surface disdrometers and assumes that surface rainfall is representative for the mean rainfall of the whole rain column. Uncertainties for CLWP retrievals are estimated to range from 200 to  $250 \text{ g m}^{-2}$  for typical rain rates between  $\sim 3$  and  $4 \text{ mm h}^{-1}$  and larger errors for larger rain rates. A novel approach to simultaneously retrieving cloud and ice water paths (including

mixed layers) and mean rainfall rate by *Matrosov* [2009b] uses multifrequency radar measurements (Ka, W, and ancillary S bands) and results in values of LWP in the range of  $300\text{--}400 \text{ g m}^{-2}$  for stratiform precipitation; even values of cloud LWP above  $1000 \text{ g m}^{-2}$  are commonly found. Although those works focus on specific cases, they found on average only insignificant correlations between cloud LWP and rainfall rates.

[8] *Czekala and Simmer* [1998] first predicted the possibility to exploit the polarization difference (PD) in brightness temperatures,  $\text{PD} = \text{TB}_V - \text{TB}_H$ , produced by nonspherical raindrops to distinguish cloud water from rainwater in multispectral ground-based microwave brightness temperature measurements at vertical  $\text{TB}_V$  and horizontal  $\text{TB}_H$  polarization. The polarization signal is explained by the increasing oblateness of rain drops with size. Such particles produce negative PD which depend on observation wavelength, hydrometeor size distribution, and observation slant angle.

[9] *Czekala et al.* [2001b] provided one of the first proofs of the predicted polarization signal, and *Czekala et al.* [2001a] proposed a retrieval methodology. Inversion algorithms for ground-based radiometer retrieval for surface rain rates from ground-based radiometer observations were presented by *Marzano et al.* [2005a, 2005b]. In an even more ambitious approach, *Knupp et al.* [2009] showed the potential of microwave radiometers for profiling temperature even within precipitating cloud systems up to midtropospheric levels, but no explanation is provided about the retrieval procedure of profiles during rainy events and how the presence of raindrops is accounted for by the inversion algorithm.

[10] Recently, the fully steerable Advanced Microwave Radiometer for Rain Identification (ADMIRARI) was developed following the ideas of *Czekala et al.* [2001a]. ADMIRARI measures at 10.7, 21.0, and 36.5 GHz the vertically and horizontally polarized emitted radiation with the same beam width of about  $6.5^\circ$  (<http://www2.meteo.uni-bonn.de/admirari>). *Battaglia et al.* [2009a] showed the first ADMIRARI measurements, which proved the necessity of the multifrequency polarization signal for isolating non-Rayleigh and polarization effects; they also found that three dimensional effects need to be taken into account in order to explain the whole PD dynamics in accordance with findings by *Czekala et al.* [2001b] for convective precipitation. A detailed analysis of the different effects of emission and increasing orders of scattering on the signal was provided by *Battaglia and Simmer* [2007]. Simulated results obtained by solving the 3-D radiative transfer equation using the backward Monte Carlo technique [*Battaglia et al.*, 2007] are found to be in good agreement with a wide range of observations at the three ADMIRARI frequencies. Only a slight mismatch at 10.7 GHz was observed, which was caused by channel misalignment [*Battaglia et al.*, 2009a, Figure 5].

[11] *Battaglia et al.* [2009b] developed a first approach to retrieve simultaneously reasonable estimates of integrated water vapor, rain and cloud liquid water path from the six ADMIRARI observables under rainy conditions. Their Bayesian inversion method exploits a large set of realizations of the Goddard Cumulus Ensemble (GCE) Cloud Resolving Model (CRM) to establish a prior probability density function of rainfall profiles. Finally, *Battaglia et al.*

[2011] have shown unprecedented observations from ADMIRARI of tropical heavy rain cells from a recent field campaign in Brazil highlighting the importance of introducing 3-D and nonuniform beam filling (NUBF) effects in the radiative transfer calculation in order to reproduce the observed microwave signatures.

[12] In the current study an improved algorithm for the inversion of ADMIRARI observables is presented and applied to a longer measurement period in order to analyze the general behavior of cloud LWP, rain LWP (RLWP), and integrated water vapor (IWV) during midlatitude autumn rain events. In section 2, the experimental setup is described along with the collected database. Section 3 outlines the newly expanded Bayesian algorithm which exploits the rain spatial structure as observed by a micro rain radar attached to the radiometer [see *Battaglia et al.*, 2009a, Figure 1]. Section 3 also includes an in-depth simulation-based error analysis. Section 4 presents results both for a case study and for a longer measurement period with emphasis on the partitioning statistics of cloud and rain LWP. Section 5 contains a summary of our results with major conclusions and an outlook. Appendix A summarizes the comparison of pure radar-based rain retrieval results with the Bayesian ADMIRARI results.

## 2. Field Campaign and Instrumentation

[13] ADMIRARI has been continuously measuring from 5 May to 12 December 2008 at the Cabauw Experimental Site for Atmospheric Research observatory (CESAR) in the Netherlands in the frame of the European integrated project on aerosol, cloud, climate, and air quality interactions (EUCAARI) campaign. Microwave radiometry for cloud investigations at Cabauw was initiated in 2001 in the framework of the first BALTEX Bridge Campaign (BBC) [see *Crewell et al.*, 2004]. During EUCAARI ADMIRARI was deployed together with a MRR, which was measuring reflectivity profiles along the slant view of ADMIRARI at 30° elevation. The MRR is a compact FM-CM radar usually deployed for vertical sensing of raindrop size distribution (DSD) profiles derived from the Doppler signal. From the DSD binned into 31 range gates representing different size intervals both the rain rate and the liquid water content are derived [*Meteorologische Messtechnik GmbH*, 2005]. Since the MRR was operating at slant view, the Doppler signal is composed by both vertical and horizontal components of the rainfall velocity and since the built-in MRR software assumes a empirical relationship between raindrops falling velocity and drop size, the standard MRR products, e.g., liquid water content (LWC), rain rate, etc., could not be used because of the unknown horizontal wind component, i.e., DSDs could not be retrieved. This non-standard off-zenith operational setup required the development of a new software package to compute the radar equivalent reflectivity from the raw spectral power after estimating the receiver spectral noise level following procedures described by *Meteorologische Messtechnik GmbH* [2005]. As an additional reference for the noise an average spectral noise level has been obtained from clear sky measurements, thus eventual noise overestimations can be avoided. The derived algorithm was also applied in the study by *Kneifel et al.* [2011], who evaluated the potential

of the MRR for snow fall retrieval. Because of a communication problem between the electronic unit and the logging computer, MRR data are only available from August to November 2008.

[14] The radiometer observations were quality checked and cases of obvious radio interferences and direct Sun overpasses within the instrument field of view were discarded. In order to avoid measurements with likely wet antennas, the CESAR wind direction observations were used to remove cases when the radiometer was pointing to upwind directions. ADMIRARI's data were flagged by means of the MRR detection of rain within the same line of sight; because of the unequal time resolution of both instruments (1 and 10 s for ADMIRARI and MRR, respectively) it has been given a window of  $\pm 10$  s before and after a MRR profile has been measured. Therefore, the MRR rain flag is extended to two consecutive measurements to cover the radiometer data. In addition, this procedure has been cross checked with the radiometer's in situ rain sensor in order to avoid false flagging.

## 3. Retrieval Technique

[15] Our retrieval technique is based on the Bayesian approach as realized, e.g., by *Kummerow et al.* [1996], *McFarlane et al.* [2002], and *Battaglia et al.* [2009b] and includes MRR information as an additional physical constraint. The following first describes the retrieval technique; then the generation of the database from forward model simulations is explained, and finally the retrieval performance is assessed via a sensitivity simulation study.

### 3.1. Bayesian Retrieval

[16] Bayesian theory is a general approach for solving inverse problems, i.e., the estimation of the true state of the atmosphere from indirect observations given a priori information on the expected atmospheric state. In our application the measurement vector  $\mathbf{y}_O$  contains spectral brightness temperatures and related polarization differences, which are assumed to be afflicted with random errors described by an error covariance matrix  $\mathcal{O}$ . The atmospheric state vector  $\mathbf{x}$  contains the profiles of all parameters (e.g., water vapor, temperature, cloud liquid water, rainwater, DSDs, etc.), which affect the measurement vector. Bayesian theory states that the inverse problem can be related to the forward problem through a set of measurements and prior knowledge about the probability of the state vector by [see, e.g., *Marzano et al.*, 1999; *McFarlane et al.*, 2002]

$$P_{post}(\mathbf{x}|\mathbf{y}_O) = \frac{p_f(\mathbf{y}_O|\mathbf{x})p_{pr}(\mathbf{x})}{\int p_f(\mathbf{y}_O|\mathbf{x})p_{pr}(\mathbf{x})d\mathbf{x}}, \quad (1)$$

with  $P_{post}(\mathbf{x}|\mathbf{y}_O)$  the conditional probability of the state vector  $\mathbf{x}$  given the observations  $\mathbf{y}_O$ ,  $p_{pr}(\mathbf{x})$  the a priori probability of the state vector  $\mathbf{x}$  before the measurement is made, and  $p_f(\mathbf{y}_O|\mathbf{x})$  the conditional (or forward) probability of the measurement  $\mathbf{y}_O$  given the state vector  $\mathbf{x}$ .

[17]  $p_f(\mathbf{y}_O|\mathbf{x})$  can be modeled from the distribution of observations close to the simulated synthetic observation  $\mathbf{y}_S(\mathbf{x})$ , with the width of the distribution governed by the measurement and the model errors. If these errors can be

assumed to be Gaussian and uncorrelated, then the probability of observational deviations may be expressed as

$$p_r(\mathbf{y}_O | \mathbf{x} = \mathbf{x}_{\text{true}}) \propto P([\mathbf{y}_O - \mathbf{y}_S(\mathbf{x})]), \quad (2)$$

with

$$P([\mathbf{y}_O - \mathbf{y}_S(\mathbf{x})]) \propto \exp\left\{-\frac{1}{2}([\mathbf{y}_O - \mathbf{y}_S(\mathbf{x})]^T(\mathcal{O} + \mathcal{S})^{-1} \cdot [\mathbf{y}_O - \mathbf{y}_S(\mathbf{x})])\right\} \quad (3)$$

where  $\mathcal{S}$  is the error covariance matrix of the simulation. For simplification we denote the residuals as

$$[\mathbf{y}_O - \mathbf{y}_S(\mathbf{x})]^T(\mathcal{O} + \mathcal{S})^{-1}[\mathbf{y}_O - \mathbf{y}_S(\mathbf{x})] = \delta^2. \quad (4)$$

When substituting equations (3) and (4) into (1) the posterior PDF may be rewritten as

$$P_{\text{post}}(\mathbf{x} | \mathbf{y}_O) = \frac{\exp(-\frac{1}{2}\delta^2)p_{pr}(\mathbf{x})}{\int \exp(-\frac{1}{2}\delta^2)p_{pr}(\mathbf{x})d\mathbf{x}}. \quad (5)$$

To obtain the expected (in the adopted formulation the mean) state vector, the state vector  $\mathbf{x}$  is integrated over its phase space weighted with the posterior PDF, i.e.,

$$\langle \mathbf{x} \rangle = \int \mathbf{x} P_{\text{post}}(\mathbf{x} | \mathbf{y}_O) d\mathbf{x}. \quad (6)$$

The second moment of the posterior PDF gives an estimation of the retrieval uncertainty, namely the variance around the mean vector  $\langle \mathbf{x} \rangle$

$$\sigma_{\mathbf{x}}^2 = \int (\mathbf{x} - \langle \mathbf{x} \rangle)^2 P_{\text{post}}(\mathbf{x} | \mathbf{y}_O) d\mathbf{x} \quad (7)$$

[18] Thus, in a Bayesian approach a measurement refines previous knowledge of the physical parameters by narrowing their probability distribution function moving from an a priori probability  $P_{pr}$  to a posterior PDF (equation (5)) of the variables that are retrieved. The Bayesian method also allows the determination of the “additional value” added by a measurement via the entropy concept. The entropy of a PDF relative to the a priori knowledge of the system (relative entropy) is defined by [Rodgers, 2000]

$$S(P) \equiv - \int P(x) \ln \left[ \frac{P(x)}{P_{pr}} \right] dx. \quad (8)$$

The additional information provided by a measurement is proportional to the reduction in entropy, i.e., the difference between the entropy before and after taking the measurement, i.e.  $H = S_1(P) - S_2(P)$ . Since the knowledge about a system before the measurement relies only on the a priori PDF its relative entropy is zero ( $S_1(P) = 0$ ). When a measurement is made the information content is augmented by the relative entropy [Rodgers, 2000; McFarlane et al., 2002]

$$H = \int P_{\text{post}}(\mathbf{x} | \mathbf{y}_O) \ln \left[ \frac{P_{\text{post}}(\mathbf{x} | \mathbf{y}_O)}{P_{pr}(\mathbf{x})} \right] d\mathbf{x} \quad (9)$$

When the observation adds information to the retrieval, the posterior PDF occupies a small portion of the a priori PDF and the relative entropy  $H$  is positive.

[19] In the following we assume that the measurement and model errors are uncorrelated between the different frequencies, and thus the covariance matrices become diagonal with variances driven by the instrument and simulation errors; nevertheless, the latter can be considered as a questionable assumption since the model errors are likely correlated (assumption 1). We further assume that the state profiles in the model database occur roughly with the same relative frequency as those found in the climatological regime where the inversion method is applied (assumption 2). It follows that the probability of occurrence of a given state profile in (5) is roughly the same (e.g.,  $p_{pr}(\mathbf{x})$ ) as those naturally occurring [Kummerow et al., 1996].

[20] In order to satisfy the second assumption, not only a sufficiently large and representative database of atmospheric state profiles is mandatory, but also a proper definition of the a priori PDF of the simulations. In the current scheme each CRM profile in the database is used to produce a set of microphysical state and observation geometry configurations [Battaglia et al., 2009b], resulting in  $\sim 10^6$  state profiles in the database.

[21] The retrieval state vector  $\mathbf{x}$  contains, among the detailed profiles, the integrated water vapor, the cloud liquid water path, and rain liquid water path, while  $\mathbf{y}_O$  either comprises the three ADMIRARI TBs at vertical polarization and the three related PDs, i.e.,  $TB_V - TB_H$  in a pure radiometer retrieval approach, or includes also the  $Ze(r)$  slant reflectivity profiles in a combined radiometer-radar approach. In the following sections these two definitions of the measurement vector are denoted as RAD when  $\mathbf{y}_O = [TB_i \text{ PD}_i]$  and RADMRR when  $\mathbf{y}_O = [TB_i \text{ PD}_i \text{ Ze}_r]$ , with  $i$  counting for the three ADMIRARI frequencies and  $r$  indicating the MRR range. As stated by Battaglia et al. [2009b, equation (6)], a quality index (QI) is adopted to assess the closeness between observations and simulations. QI is defined as  $QI \equiv \min\{\delta^2\}$  with the minimum determined by a search over the selected a priori subdatabase and  $\delta^2$  given by equation (4).

[22] As a new addition to the algorithm additional constraints are imposed on the a priori profiles by exploiting the MRR observations of slant path reflectivity. Because of the different spatial radial resolutions between profiles from the MRR (300 m) and the synthetic hydrometeor profiles (1 km for the slant observation) a more stringent selection based on the geometry of the synthetic rain was not possible.

[23] The constraint is applied by attributing each observation to one of three scenarios: (1) no rain is observed; (2) the rain layer extends all the way down to the radiometer, and thus ADMIRARI is situated within the rain volume; and (3) the rain cell is located at a certain distance from the radiometer, and thus the radiometer is outside the rain volume. The a priori selected synthetic data subset is composed only of simulations with profiles classified according to the MRR observations. Thus the retrieval avoids radiometrically similar profiles which significantly differ in spatial structure from the observed profile.

### 3.2. The Retrieval Database

[24] CRM simulations available from the GCE have been extensively applied to study cloud-radiation interaction, cloud-radiation-climate relations and to develop rain retrieval algorithms for the Tropical Rainfall Measuring Mission (TRMM). The employed cloud microphysics include a parameterized two category liquid water scheme (cloud water and rain), and a three-category ice phase schemes (cloud ice, snow, and hail/graupel). The shapes of liquid and ice particles are assumed to be spherical. Size distributions of rain, snow and graupel are taken to be inverse exponential with respect to diameter (equation (10)). The typical intercept parameters used in the GCE model for rain, snow, and graupel are 0.08, 0.04, and 0.04  $\text{cm}^{-4}$ , respectively [Tao and Simpson, 1993].

[25] In the present work radiative transfer calculations determine the synthetic measurement vector  $\mathbf{y}_s$  given an atmospheric state vector, selected as 1-D columns from the 3-D CRM GCE. The effects of a precipitating cloud with 3-D structure are included by “planting” such cloud box columns into an otherwise cloud-free environment. These columns are then “observed” from different positions within and outside the precipitating column by an ADMIRARI-like radiometer taking into account the 6° antenna beam width. With eight observation positions (four inside and four outside the cloud), a single CRM hydrometeor profile is mapped into eight observed slant profiles producing eight different integrated water contents. Thus variability along the slant path is only produced by the vertical variability within individual columns of the CRM database and by the viewing geometry, but not (yet) by the “true” horizontal variability within the CRM scene. These geometrical 3-D simulations are supplemented by 1-D simulations based on the fast RT4 code [Evans and Stephens, 1991] which assumes a horizontally infinite homogeneous medium. One-dimensional simulations are considered adequate when the radiometer is located inside a stratiform rain extending horizontally for more than 4 km, which is the largest extension considered by the box type cloud model.

[26] Since the GCE CRM provides no information about the shapes of raindrops, we assume for the radiative transfer simulations mass equivalent oblate spheroids with preferential horizontal alignment. The axis ratio is computed as a function of the equivalent spherical raindrop diameter  $D_e$  according to  $\mathcal{A} = 1.0 + 0.05b - bD_e$ , for  $D_e < 0.05$  cm with the shape factor  $b$  set to 0.6  $\text{cm}^{-1}$ . Battaglia *et al.* [2009b] have shown that the range of the shape factor  $b$  from 0.5 to 0.7  $\text{cm}^{-1}$  has a marginal influence on the brightness temperature and polarization difference compared to effects produced by different DSD assumptions.

[27] The single corresponding scattering properties i.e., the extinction and the scattering matrices, and the emission vector are computed with a T matrix method. The Earth surface is assumed to be Lambertian with emissivity equal to 0.9. [Battaglia *et al.*, 2006, 2009b]. Drop size distributions are modeled according to the inverse exponential distribution

$$N(D) = N_0 \exp(-\Lambda D). \quad (10)$$

Since the DSDs influence the polarization difference, four intercept parameters  $N_0$  are considered in order to cover

different rain regimes: light rain with  $N_0 = 32.0 \times 10^3 \text{ m}^{-3} \text{ mm}^{-1}$ , Marshall-Palmer with  $N_0 = 8.0 \times 10^3 \text{ m}^{-3} \text{ mm}^{-1}$ , heavy rain with  $N_0 = 4.0 \times 10^3 \text{ m}^{-3} \text{ mm}^{-1}$  and thunderstorm-type rain with  $N_0 = 1.4 \times 10^3 \text{ m}^{-3} \text{ mm}^{-1}$ . The last category has been added recently as an attempt to accommodate the large spread in the observed polarimetric signatures.

[28] Finally for each radiometric observation point, its corresponding slant profile of the attenuated reflectivity as measured by a MRR-like radar has been computed via Mie theory and imposing the DSD described above (equation (10)). The radiometer position (and thus of the MRR) relative to the rain cell, the finite thickness of the rain layer and the attenuation modulated by the cloud structure have been accounted for. Then the simulated reflectivity is given by

$$Z_m(s) = Z(s) - 2 \int_0^s A_{tot}(r) dr, \quad (11)$$

with  $Z(s)$  the radar reflectivity factor at range  $s$ , as derived from equation (A1) and expressed in dBz and  $A_{tot}(r)$  ( $\text{dB km}^{-1}$ ) the total attenuation:

$$A_{tot}(r) = 10 \log_{10}(e) \left[ A_{gases}(r) + 6\pi \nu q_c(r) \frac{\text{Im}\{\epsilon_w\}}{|\epsilon_w + 2|^2} + \int_0^\infty N_{rain}(D, r) \sigma_{ext}^{MIE}(D) dD \right] \quad (12)$$

decomposed into the attenuation due to gases (oxygen, dry air, and water vapor), cloud, and rain, with  $\epsilon_w$  being the dielectric constant of water at the given frequency and temperature.

### 3.3. Retrieval Sensitivity Study

[29] The expected retrieval performance was assessed by a simulation-based sensitivity study. For that purpose a subset of states was identified and removed from the simulations database. The corresponding simulated radiation temperatures were perturbed by a random Gaussian instrument error with a RMS of 0.5 K and treated as virtual radiometer measurements. The range resolution of the simulated MRR measurements (i.e., attenuated reflectivity profiles) were interpolated to 300 m to match a typical measurement range.

[30] Figure 1 depicts 660 samples of synthetic ADMIRARI measurements, as they were “observed” at 30° elevation angle. The profiles in Figure 1 contain a random selection of simulations but sorted according to their DSDs and the positions of the clouds relative to the radiometer. Thus, the sequence of simulated measurements in Figure 1 does not intend to represent the development of natural rain events with time or the full range of possible observations. In this study only states with freezing levels between 2.5 and 3.5 km (see black line in Figure 1, top) are considered in order to confine the actually used states in the simulation data base to atmospheric conditions prevailing during the EUCAARI measurements.

[31] In order to perform an independent retrieval performance evaluation, the states extracted for the generation of measurements were removed from the a priori database. The analysis follows several steps. First the retrieval algorithm is

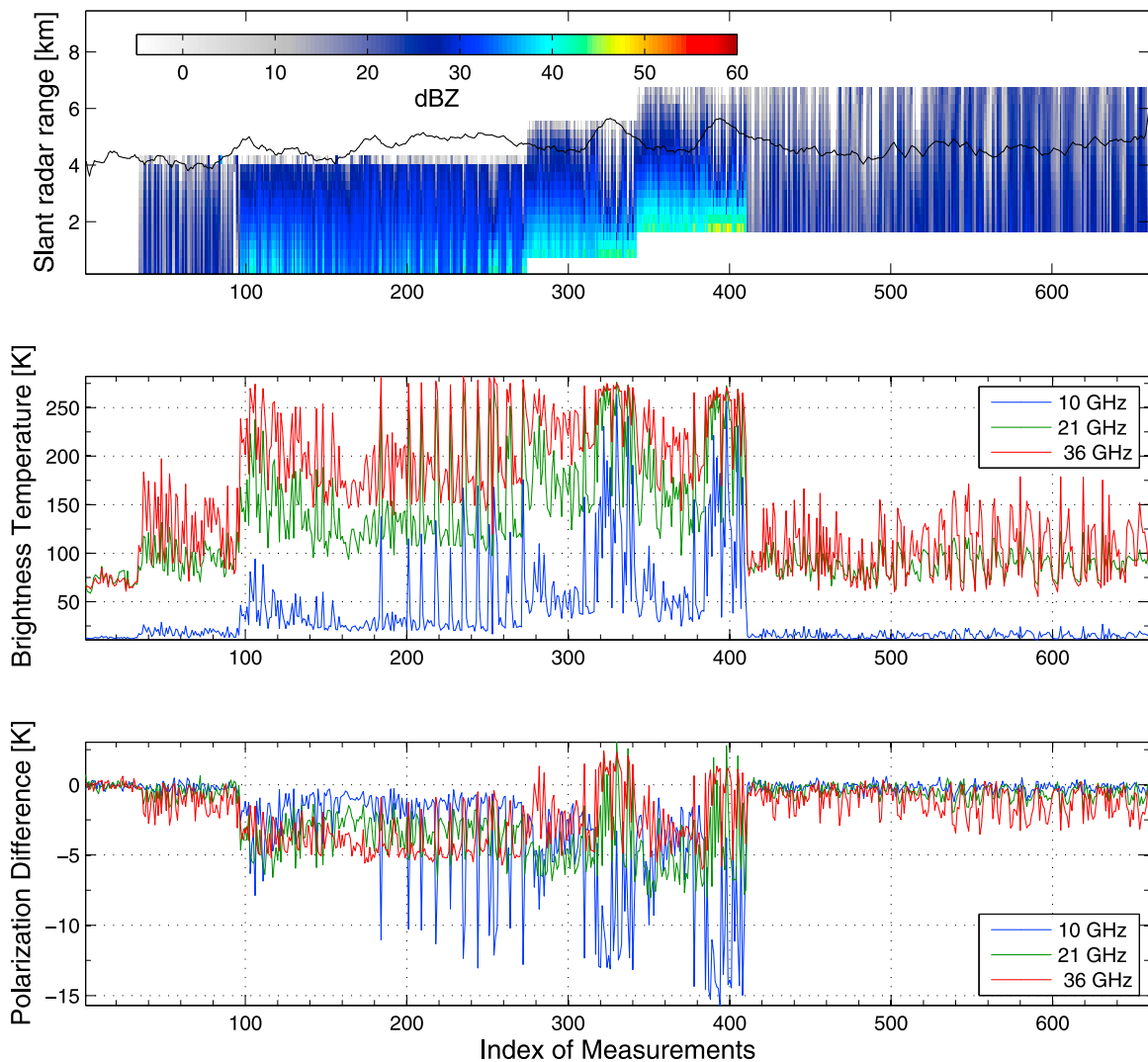


**Figure 1.** Synthetic measurements selected to test the retrieval technique. (top) Radar attenuated reflectivity. The  $0^\circ$  isoline is indicated by the black line. (middle) Brightness temperature. (bottom) Polarization difference at the three Advanced Microwave Radiometer for Rain Identification (ADMIRARI) frequencies.

applied to passive radiometric information only, i.e., TBs and PDs (referred to as RAD). Then the MRR reflectivity profile is incorporated to the Bayesian retrieval in a combined radiometer-radar method (referred to as RADMRR). A complementary study assesses the impact of degrading the radiometer from triple to dual frequency (e.g., 10 and 21, 10 and 36, and 21 and 36 GHz, referring to RAD 10 and 21 and so forth).

[32] Figure 2 compares the retrieved cloud and rain LWP and IWV against their corresponding true values for the five retrieval variants. Figure 2 (left) depicts the retrievals with all six radiometric channels without (RAD, blue boxes) and with the radar combined (RADMRR, green pluses). Figure 2 (right) presents the results for the dual-frequency degradation approach. Table 1 lists the corresponding root-mean-square errors (RMSE) separately for the different DSD assumptions. RADMRR leads to retrievals with the least number of outliers in line with the expectation, that

geometrical information about the distribution of the rain-water reduces ambiguities in radiometric measurements.

[33] The degradation to dual-frequency retrievals always lower the retrieval performance for all frequency combinations. The relevance of the 10 GHz channel for rain retrieval is highlighted by the poor performance of the 21–36 GHz combination, specially when heavy rain is present. This is also indicated in Table 1 by the largest RMSE obtained for the couple 21–36 GHz. The worst results for IWV retrievals are, as expected, when the 21 GHz (close to the weak water vapor rotation line) is absent.

[34] In Figure 3 the absolute errors for all retrieval schemes are summarized by box plots. Every box plot indicates the distribution of absolute errors by its median (red mark) and its 25th and 75th percentiles (bottom and top edges of the box); the blue crosses indicate the outliers. In general, the triple and dual-frequency pure radiometer retrieval approaches differ, predominantly, in the distribution of the absolute error rather than in their median values.

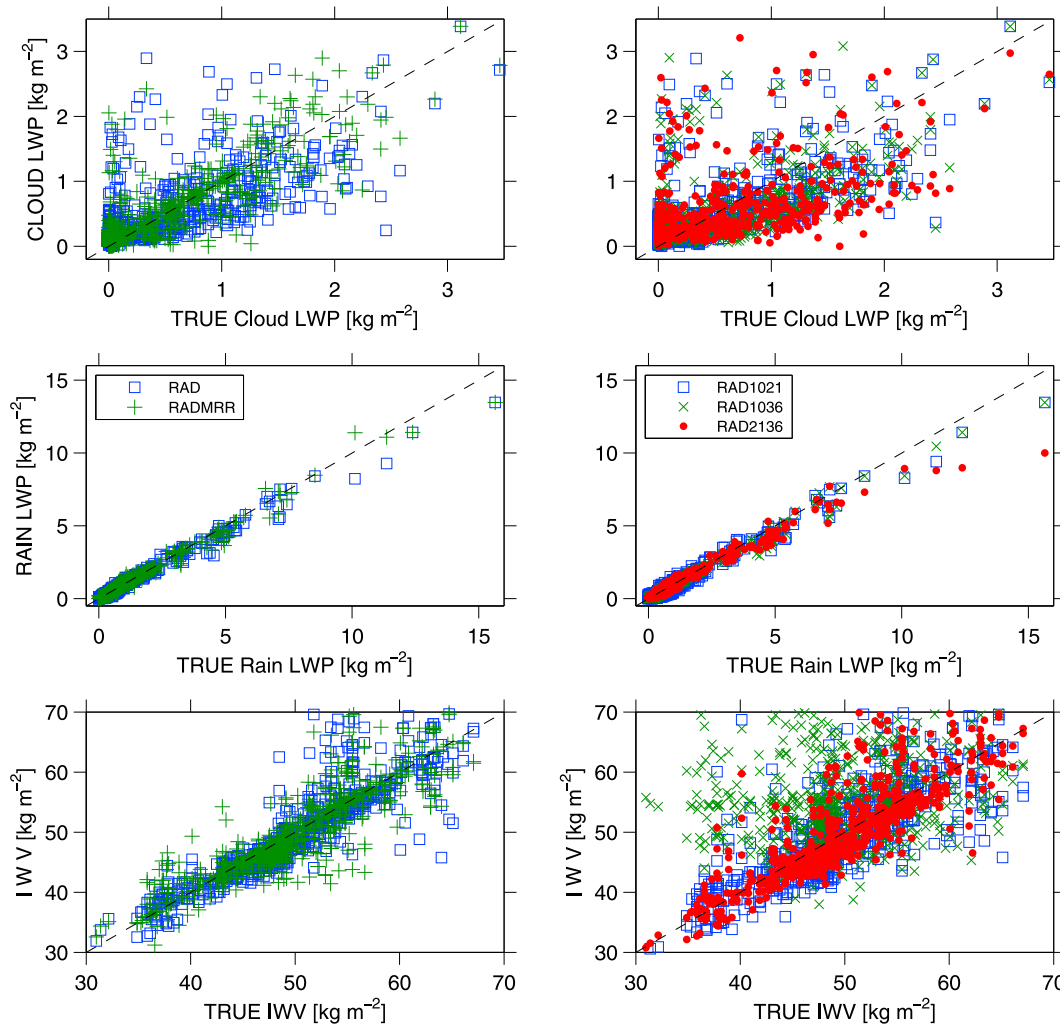


**Figure 2.** Scatterplot for retrieval versus true values for (top) cloud, (middle) rain, and (bottom) water vapor. (left) Pure radiometer (RAD) and radar-radiometer combined technique (RADMRR) and (right) the combination of only two frequencies.

Including the radar reflectivity profile to the retrieval leads to a systematic and significant reduction in the variance when comparing the pure radiometer and the radiometer-radar approaches. The latter is mirrored by a 98%, 86%, and

84% reduction on the median absolute error for rain, cloud and water vapor correspondingly. For the retrieval of IWV the MRR incorporation has only a low impact on the spread of the errors distribution compared to the pure radiometer

**Table 1.** RMSE for IWV ( $\text{kg m}^{-2}$ ), CLWP ( $\text{g m}^{-2}$ ), and RLWP ( $\text{g m}^{-2}$ ) Resulting From the Retrieval Sensitivity Study Normalized to Zenith Observations<sup>a</sup>

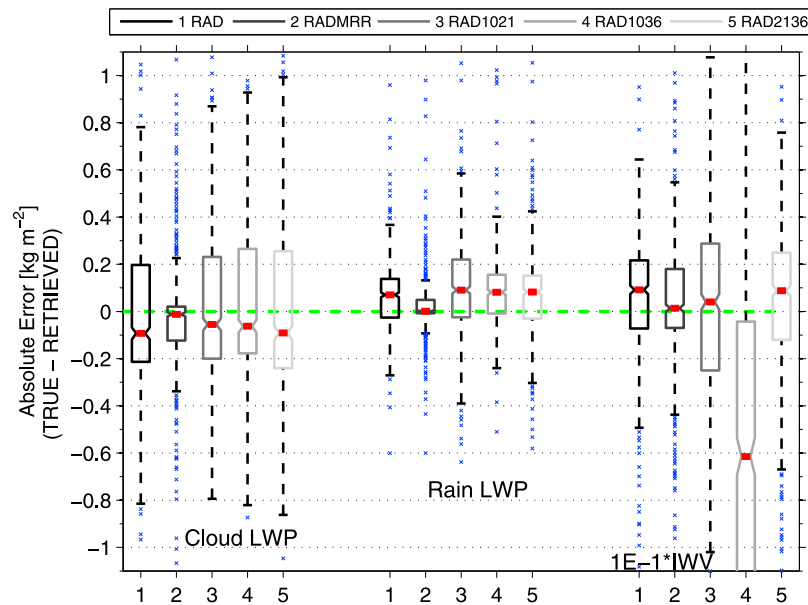
	RAD			RADMRR			RAD 10 and 21			RAD 10 and 36			RAD 21 and 36		
	IWV	CLWP	RLWP	IWV	CLWP	RLWP	IWV	CLWP	RLWP	IWV	CLWP	RLWP	IWV	CLWP	RLWP
TS	0.84	121.5	34.4	0.68	76.5	18.2	1.05	133.6	41.9	1.67	120.8	31.3	1.40	154.9	87.2
HR	1.16	126.5	87.6	0.94	106.4	70.7	1.61	137.6	94.7	2.62	145.9	86.1	1.46	144.7	134.8
MP	1.04	127.5	74.8	0.99	97.8	57.6	1.58	117.9	90.7	3.75	131.7	79.8	1.04	132.7	76.9
LR	0.65	91.2	47.2	0.57	40.5	22.1	1.08	88.1	65.9	4.93	96.3	46.3	0.72	111.8	55.6

	RAD		RADMRR		RAD 10 and 21		RAD 10 and 36		RAD 21 and 36	
	IWV	TLWP	IWV	TLWP	IWV	TLWP	IWV	TLWP	IWV	TLWP
TLWP <sup>b</sup>	1.61	45.7	1.59	13.5	2.08	48.4	6.76	53.4	2.22	40.0

<sup>a</sup>Drop size distributions: TS, thunderstorm; HR, heavy rain; MP, Marshall-Palmer; LR, light rain. RMSE, root-mean-square error; IWV, integrated water vapor; CLWP, cloud liquid water path; RLWP, rain liquid water path. See text for definition of RAD and RADMRR.

<sup>b</sup>RMSE for retrievals of total liquid water path (TLWP) ( $\text{g m}^{-2}$ ) below  $450 \text{ g m}^{-2}$ .



**Figure 3.** Absolute errors box plots for cloud, rain, and water vapor obtained from the retrieval sensitivity study. The approaches RAD, RADMRR, 10 and 21, 10 and 36, and 21 and 36 are numbered from 1 to 5, respectively. The red mark indicates the median, the first and third quartiles correspond to the box's bottom and top edges, the black bars show the  $3\sigma$  interval, and the blue crosses are the outliers.

mode, and larger errors are found when only two frequencies are used utterly severe when the 21 GHz is absent.

[35] The relative error of the rain-cloud partition  $[(LWP_{\text{true}} - LWP_{\text{ret}})/LWP_{\text{true}}]$  retrieval from the RAD and RADMRR approaches are presented in Figure 4; only results with both cloud and rain components are included (i.e., CLWP and RLWP greater than 0). For large cloud water or rainwater contents, the retrieval performs reasonable (see the accumulation of large square marks scattered around the 0-0 intersection). In general, however, the error distribution shows a clear tendency toward underestimation and overestimation for rain and cloud contents, respectively. For RADMRR the improvement compared to RAD in the relative error is accompanied by an increase of points close to the 0-0 intersection, in particular for the rain component; the larger relative errors at low cloud and rain contents are similar for RAD and RADMRR approaches.

[36] The occurrence of extreme relative overestimation errors for the cloud component (Figure 4) suggests that LWP retrievals with relative errors exceeding 50% are much more likely to occur for cloud than for rain (see the spread of the wide relative error histogram for cloud in contrast to the narrower histogram for rain). For cloud (rain) LWP, 65% (13%) of the retrievals lead to errors above 50% for the RAD approach while for RADMRR only 47% (1%) is obtained.

[37] For very low liquid water contents the inversion does not properly reproduce the cloud-rain partition. Simulations show that for light rain, most raindrops are too small to produce significant polarization; e.g., the polarization difference at  $30^\circ$  elevation is not larger than  $-0.5$  K at the most sensitive 36.5 GHz channel for rainwater contents up to  $120$   $\text{g m}^{-2}$ . Accordingly, the instrument noise level does not allow us to distinguish between cloud water and rainwater contents on the basis of the polarization signal.

[38] For total liquid water contents (TLWP) below  $450$   $\text{g m}^{-2}$  the RMSE of the retrieval is, on average,  $45.7$   $\text{g m}^{-2}$  when only radiometric channels are used (RAD) but decrease to  $13.5$   $\text{g m}^{-2}$  when the MRR is added (RADMRR); see Table 1. The 21 and 36.5 GHz dual-frequency approach, however, leads with an RMSE of  $40$   $\text{g m}^{-2}$  to a slightly improved result compared to the RAD. In fact 10.7 GHz is the least sensitive frequency with low LWP, thus the channel contributes no information but noise.

[39] The information content introduced by the measurements has been estimated according to equation (9). Figure 5 depicts the relative entropy as a function of the rain and cloud LWP for the RAD, RADMRR, and RAD 10 and 21 approaches. The relative entropy in Figure 5 is expressed in bits of information by dividing the result of equation (9) by  $\ln(2)$ , which is equivalent to changing the natural logarithm in equation (8) to  $\log_2$ . Accordingly the narrowing of the a priori PDF by increasing the knowledge of the retrieved parameters is given by a factor of  $2^{\text{bits}}$  [Rodgers, 2000; McFarlane et al., 2002].

[40] Figure 5 (left) clearly highlights the information added to the retrieval by the MRR reflectivity profiles. Since the MRR is a good rain detector, its measurements improve the retrieval mainly for low rainwater contents: in these cases the radiometer polarization signature is negligible or within the instrument noise and the MRR represents the only mean to separate both components. As the rain content increases the relative entropy tends to stay constant for values ranging from  $0.5$  to  $2$   $\text{kg m}^{-2}$  rain LWP followed by a drop to similar levels as the RAD approach for rain contents above  $10$   $\text{kg m}^{-2}$ . Then the radar signal is basically fully attenuated and does not add any information to the retrieval. For the radiometer-only approach measurements add the most information in the range between  $0.5$  to  $4$   $\text{kg m}^{-2}$ . As a

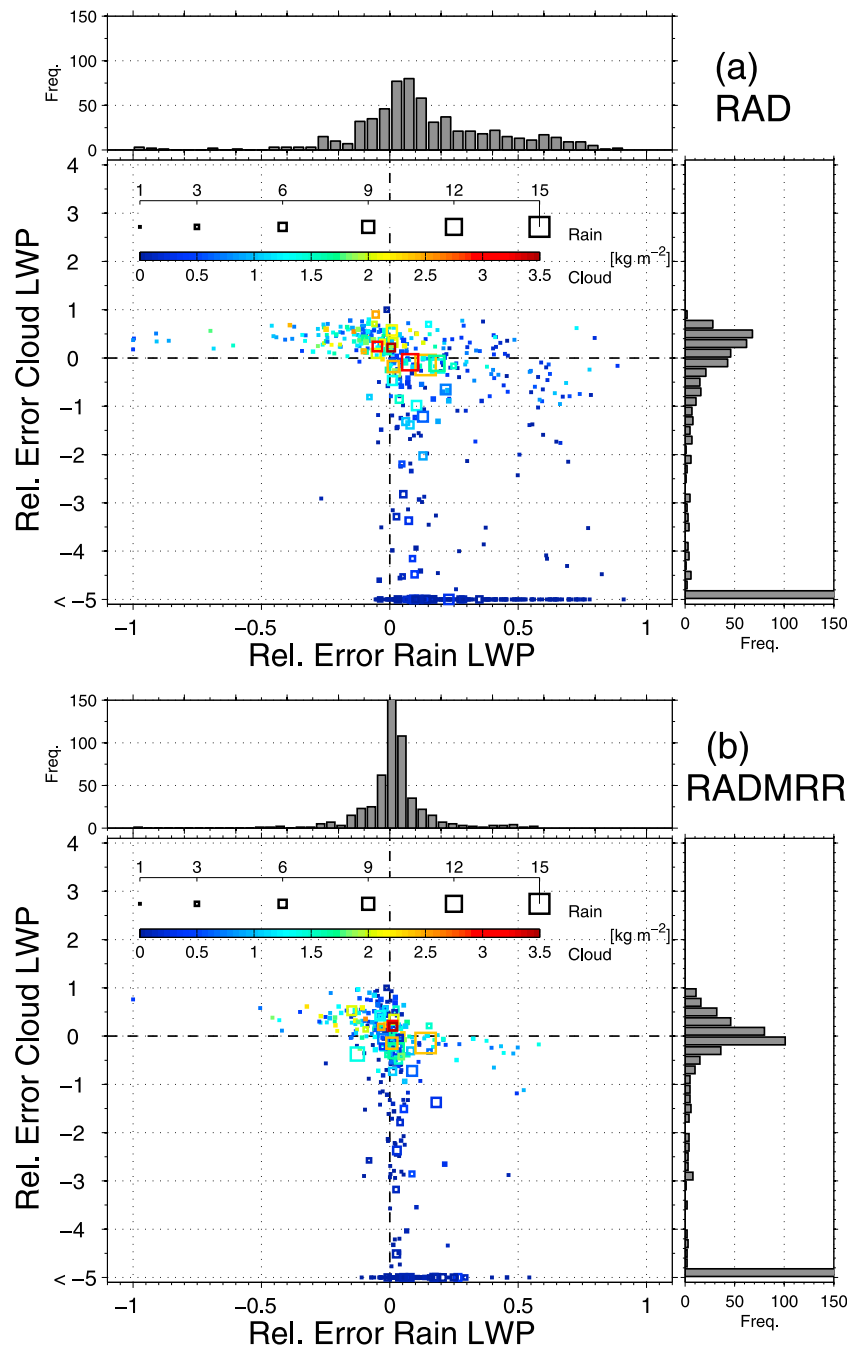


**Figure 4.** Relative error ( $\frac{LWP_{true} - LWP_{ret}}{LWP_{true}}$ ) for cloud versus rain for (a) RAD and (b) RADMRR. The color modulates the cloud component, and the square size modulates the rain component as shown above the color scale. The distribution of relative errors for cloud and rain are shown in the right and top panels, respectively.

reference when the 36.5 GHz channel is absent the information content remains low until  $1 \text{ kg m}^{-2}$ .

[41] Figure 5 (right) indicates no specific range of cloud LWP for the RAD approach where the information stands significantly out, with only a slight increase for values from 0.8 to  $2 \text{ kg m}^{-2}$ . When the radar measurements are incorporated in the retrieval (RADMRR), a well defined hump is observed between 0.6 to  $2 \text{ kg m}^{-2}$  LWP, with a fast degradation after and a very dispersed behavior before that range.

At large cloud LWP the MRR is not adding any information to the retrieval process.

## 4. Retrieval Results

### 4.1. Retrieval Example

[42] Our retrieval methodology, with the MRR as a tool to selected a priori profiles according the geometrical position and thickness of the rain layer, is applied to the case study of 10 November 2008, between 04:00 and 07:00 UTC

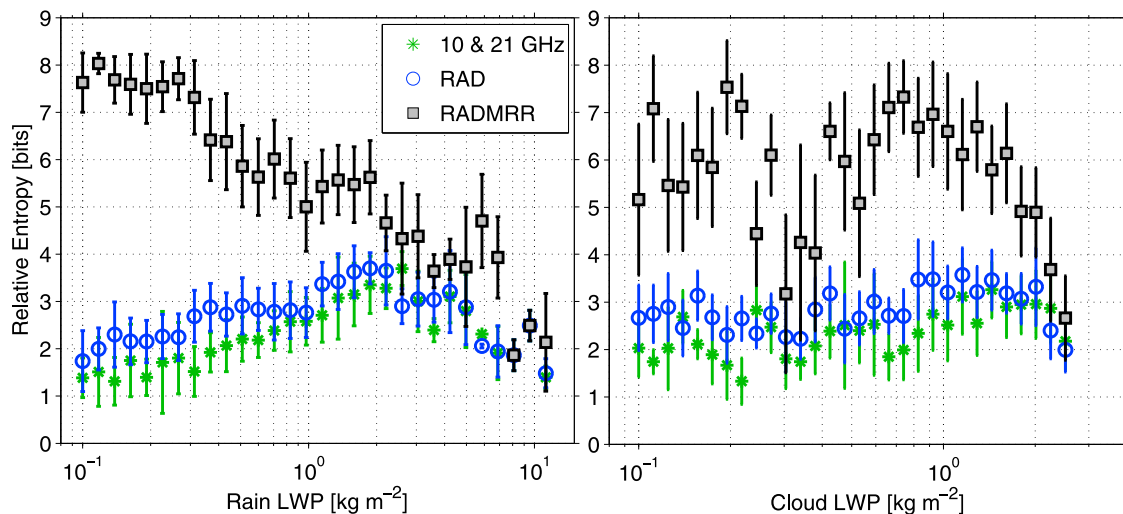


**Figure 5.** Relative entropy (a quantity indicative of the information content added by the measurement in the sensitivity study) as a function of (left) rain liquid water path (LWP) and (right) cloud LWP.

(Figure 6). The wind is blowing from azimuthal directions between  $210^\circ$  and  $250^\circ$ , while the radiometer is pointing at  $170^\circ$ . This setup ensures that the radiometer antennas were not affected by wetting. The MRR slant path reflectivity time series (first panel in Figure 6) nicely depicts a sequence of rain cells, each with its own peculiar temporal duration and spatial variability. The rain duration as detected by the rain sensor located at the radiometer (indicated by the shaded areas in Figure 6) ranges from 2 min (e.g., at 04:45 UTC) to  $\sim 30$  min (from 04:00 to 04:33 UTC). Slanted paths through rain range from  $\sim 4$  km at 04:07 UTC to  $\sim 300$  m at 05:42 UTC. The estimated freezing level from the surface temperature is also drawn as a dashed black line in the MRR reflectivity time height cross section. This case study resumes several observational scenarios that the radiometer can sense, ranging from pure cloud atmosphere to liquid and solid precipitation with different geometrical radiometer sensing positions, e.g., radiometer situated under the precipitating cloud (until 06:00 UTC) or away from it (e.g., at about 3 km distance after 06:00 UTC). Figure 7 shows the corresponding retrieval results for IWV, cloud and rain LWP together with the retrieval standard error. Hereafter all retrieval results are renormalized to equivalent vertical column values by scaling the  $30^\circ$  slant observations to zenith.

[43] From measurements in Figure 6 and their respective retrievals in Figure 7, the following features can be highlighted:

[44] 1. Measurements shows an uneven variability for both TBs and PDs, with several PD minima of  $\sim -6$  K at 36.5 GHz which do not correspond neither to minimum PDs at the other frequencies nor to similar MRR reflectivity profiles. On the other hand, when the minimum PD of  $\sim -8$  K at 10.7 GHz is observed (04:06 UTC), the 21 and 36.5 GHz depict PDs only of about  $\sim -4.2$  and  $\sim -4$  K, respectively. This stress the importance of a multifrequency approach, since every frequency reacts differently to several atmospheric regimes.

[45] 2. ADMIRARI has unique capability in distinguishing the signal from cloud and rain even when it is located far

away from the radiometer (see Figure 6 from 06:12 to 06:40 UTC). In fact when the radiometer rain sensor did not flag such events as rainy, the negatives PDs suggest the presence of rain as confirmed by the MRR reflectivity. This aspect cannot be featured by a standard single-polarized radiometer whose TBs would have been misinterpreted as coming from a pure cloud scenario, leading to inappropriate LWP values.

[46] 3. The radiometer polarization signature responds mainly to liquid precipitation composed by raindrops with horizontally oriented shapes. For instance, from 06:42 to 06:55 UTC, the radiometer PDs are negligible while the MRR detects some targets with reflectivity around 20 dBz. Such targets are however located above the  $0^\circ$  isotherm and, therefore, they likely involve precipitation in the ice phase, to which the radiometer has low or marginal sensitivity. To get a better insight into this topic ADMIRARI has recently participated to the Light Precipitation Validation Experiment (<http://lpvex.atmos.colostate.edu>) campaign.

[47] 4. ADMIRARI is capable of resolving very short rain showers like the events at 04:43 UTC and 04:45 UTC in Figure 7, with durations of only 1 and 2 min, respectively. Light rain observations from 05:06 to 05:21 UTC, where only the 36.5 GHz polarization signature is detectable, can be resolved with RLWP around  $\sim 0.15$   $\text{kg m}^{-2}$ . Even low rainwater content like  $0.05$   $\text{kg m}^{-2}$  (from 06:06 to 07:00 UTC) with coincident cloud water below  $0.1$   $\text{kg m}^{-2}$  can be retrieved. However, as discussed in section 3.3, for low water contents the partition cloud-rain LWP may be affected by large uncertainties.

[48] 5. Similar retrieval rain contents are obtained from completely different radiometric signatures. This is the case of the two peaks of  $0.55$   $\text{kg m}^{-2}$  retrieved at 04:12 UTC and 05:36 UTC in Figure 7. While the TBs in the two events are similar in magnitude at their corresponding frequencies, the PDs, which are more strongly raindrops shape and DSD dependent, are not. This pinpoints at a commonality in the macro physical property of the system under observation (i.e., same RLWP) but at disparity in the cloud microphysics (i.e., different DSDs). On the other

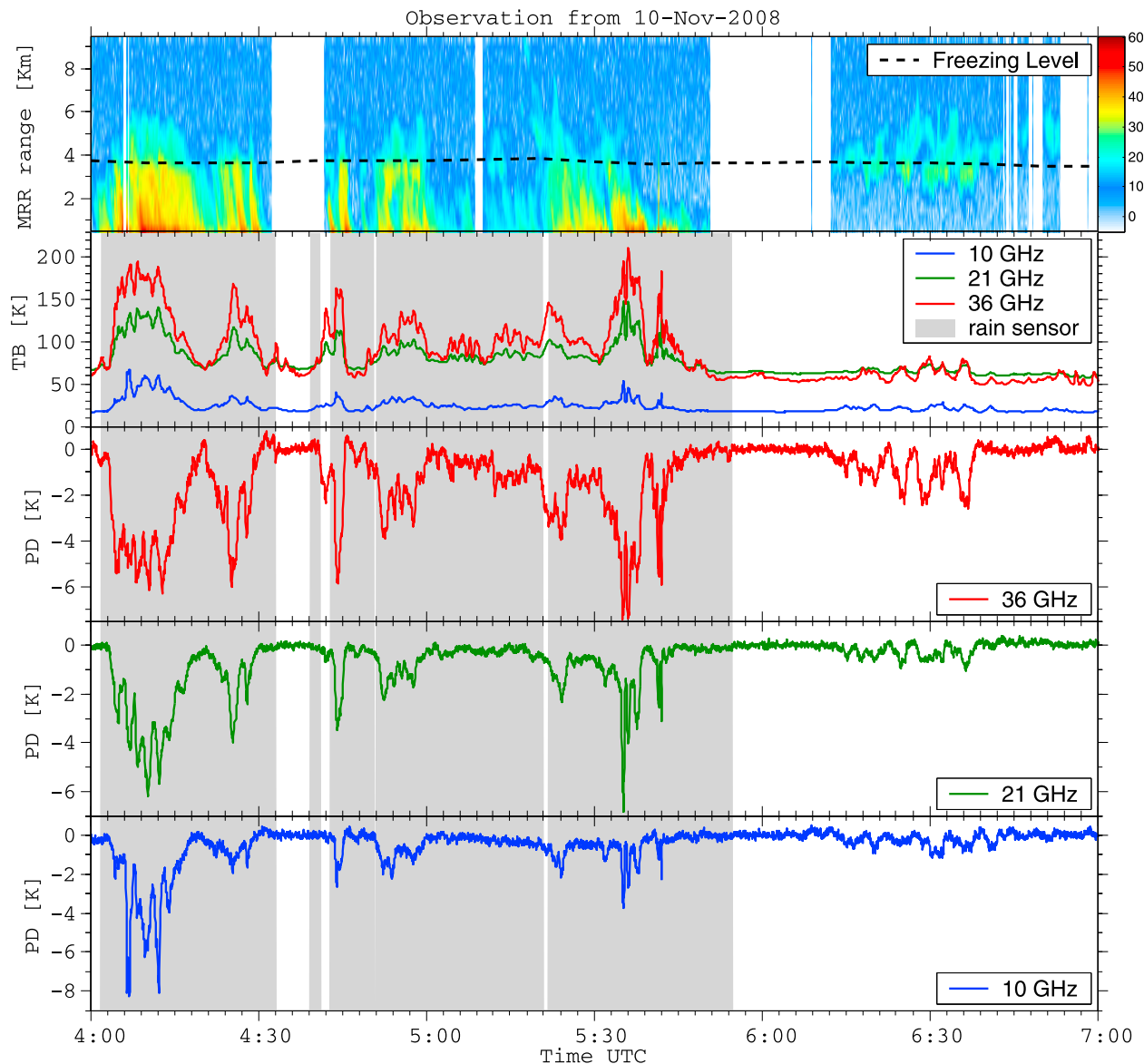


**Figure 6.** Measurements from 10 November 2008 at 30° elevation angle and fixed azimuth. The first panel shows micro rain radar (MRR) slant path reflectivity (in dBZ); the estimated freezing level is shown by the dashed black line. The second panel shows brightness temperatures for the three frequencies. The third, fourth, and fifth panels show polarization difference at 36, 21, and 10 GHz, respectively. Gray areas indicate rainy periods flagged by the rain sensor.

hand, while in the first case the radar reflectivity profile ranges from  $\sim 50$  to 30 dBZ in a rain layer of approximately 4 km, for the second case the same reflectivity range values are spread in approximately only 2 km, meaning that using a pure radar rain liquid water content retrieval, the obtained RLWP would be larger for the first case than for the second, because their integration paths are different, arising thereof a disagreement with the radiometer retrievals.

[49] 6. ADMIRARI retrieval provides information about temporal evolution of IWV during rain events. For instance, Figure 7 reveals a rapid variation of the water vapor during the rain period followed by a reduction by about  $2 \text{ kg m}^{-2}$  when the rain ceased, and by a relatively steady period even during the following rain events from 06:12 to 06:51 UTC.

Rapid fluctuations of total water vapor content during rain events were already reported by *Knupp et al.* [2009] from a vertical observation of deep convective showers with a microwave radiometer profiler.

[50] 7. The MRR is extremely useful as a “rain detector” within the slant volume observed by ADMIRARI. Nevertheless it must be mentioned that because its noise level corresponds to rain rates in the range  $0.04\text{--}0.08 \text{ mm h}^{-1}$ , it can lead to discontinuities at the transition from no-rain to rain conditions in the retrieved CLWP. In addition, its sensitivity to solid precipitation can mislead the radiometer-based retrieval and cause it to mistake liquid for solid precipitation as for the case shown in Figure 6 from 06:45 to 07:00 UTC.

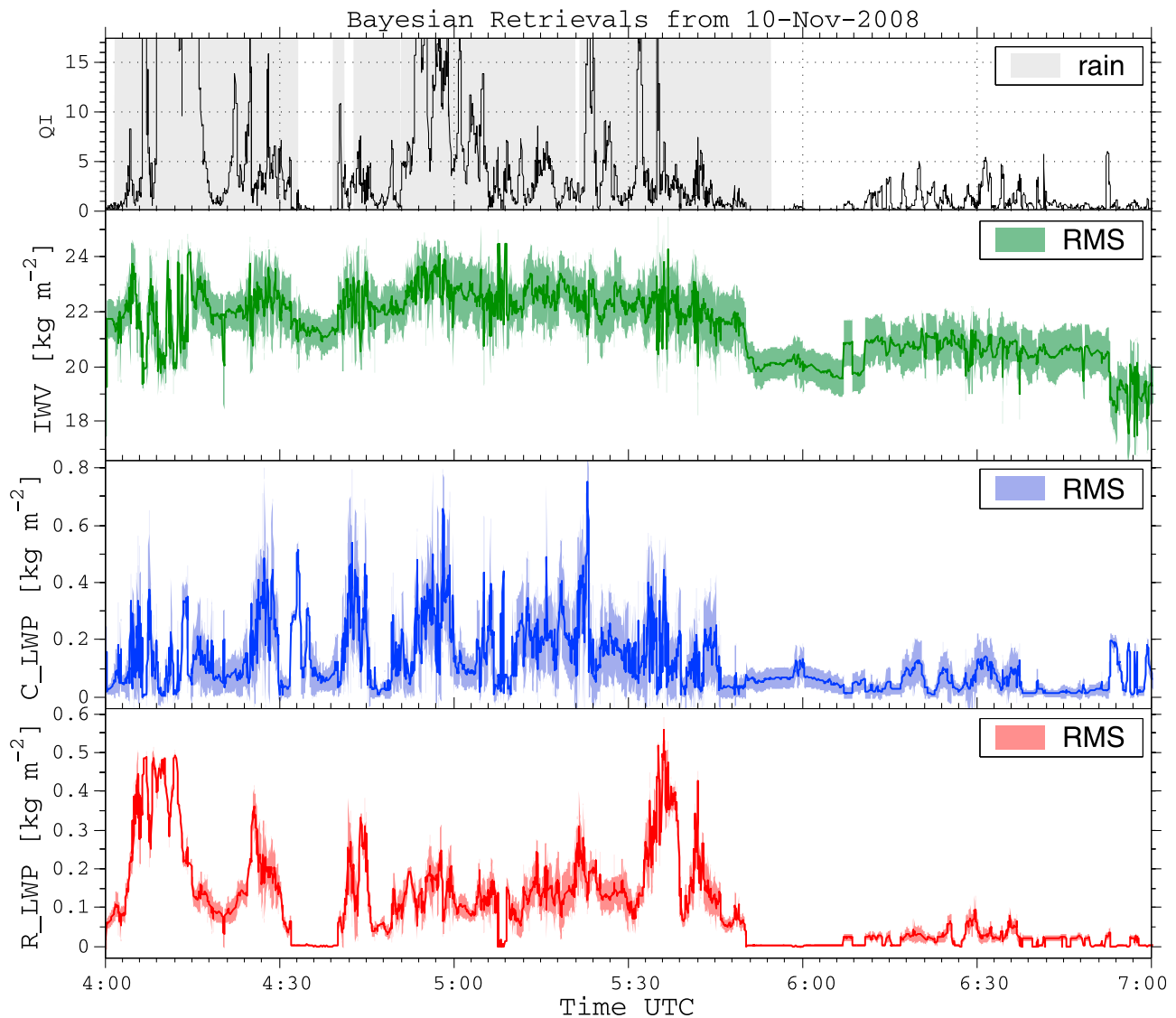


**Figure 7.** Retrieval results for the case illustrated in Figure 6. From top to bottom: quality index (QI), integrated water vapor (IWV), cloud LWP, and rain LWP. The gray area in the first panel indicates precipitation sensed by the rain sensor; colored shading shows the one standard deviation interval for the retrieved quantities.

#### 4.2. Statistical Analysis

[51] This section presents a statistical analysis of the measurements between 23 August and 12 November 2008. The observations are first filtered by a rigorous quality control procedure, which also rejects possible antenna wetting and occurrences of signal interference. Periods with high probability for antenna wetting are detected during rainy periods by analyzing the angular difference between the wind direction and the ADMIRARI observing azimuth: periods with angular differences below  $\pm 20^\circ$  are filtered out. A bias correction procedure for PDs is deemed necessary despite the radiometer internal calibration systems. The procedure first isolates periods with very low RLWP, which are expected to have negligible PD values. The corrections are then made mimicking the method used by *Gaussiat et al.* [2007], who took advantage of vertically pointing lidar

observations to discriminate between clouds and clear sky in order to avoid a bias in the cloud LWP retrieval. Here instead, the MRR observations are used to flag rain-free periods to avoid an RLWP bias during dry spells. During such periods the PDs are set to zero, and adjacent rain-free periods are used to interpolate the bias during the rainy periods in between.

[52] The time series of retrieved parameters during rainy spells is presented in Figure 8 together with observations of rain rate from a collocated gauge to enable the characterization of precipitation conditions during the measuring period. A correlation between rainfall and RLWP is apparent, but the difference between the radiometer and the gauge sampling volume makes a direct intercomparison not very meaningful, as already noted by *Marzano et al.* [2005b]. CLWP exhibits a large variability with values sometimes exceeding  $1.2 \text{ kg m}^{-2}$ . RLWP can be even higher with

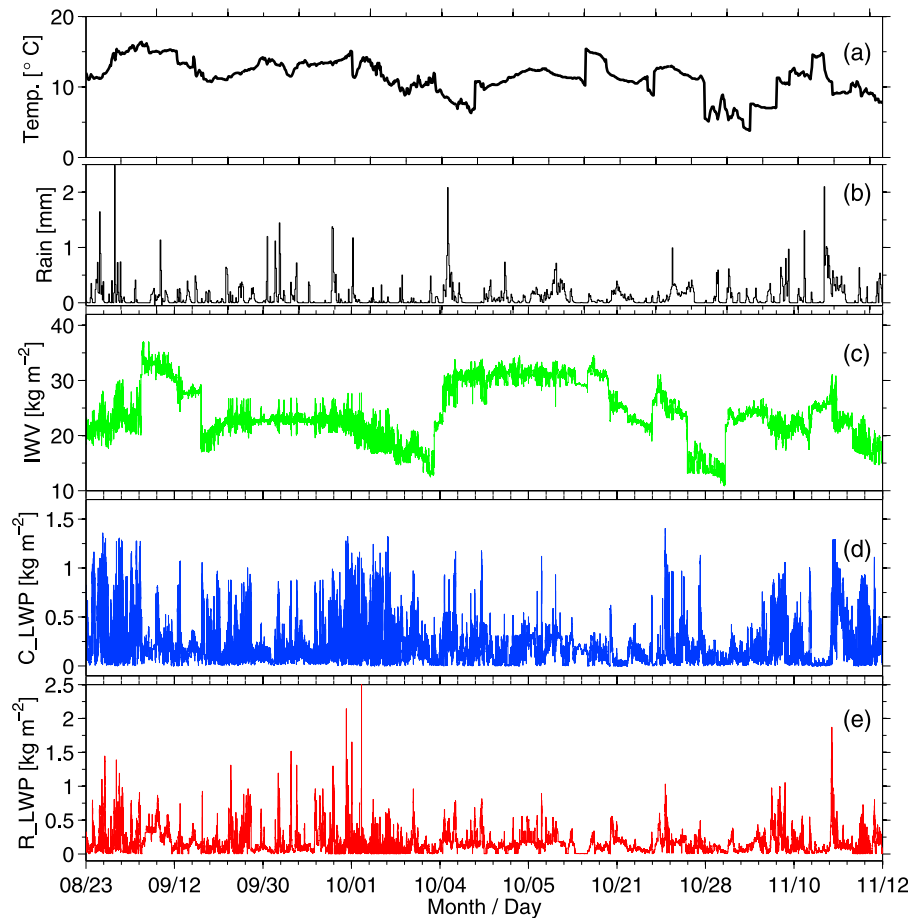


**Figure 8.** Time series of (a) 2 m temperature and (b) rain amount accumulated at 10 min intervals from a rain gauge at the Cabauw Experimental Site for Atmospheric Research observatory (CESAR); (c) retrieved IWV, (d) CLWP, and (e) RLWP from 23 August to 12 November 2008. Only rainy periods are shown.

values up to  $2.4 \text{ kg m}^{-2}$  (e.g., at the end of September and on 11 November 2008). IWV is less variable during long rainy spells (e.g., the second half of September or in October) but reveals some abrupt changes during few short periods. Those jumps are not artifacts from the retrieval algorithm but rather indicate boundaries between rain periods since rain-free periods have been taken out. Air temperatures measured at 2m (Figure 8a) are well correlated with IWV, as expected.

[53] The occurrence distribution of retrieved parameters (derived for all cases with  $\text{QI} < 20$ ) is displayed in Figure 9 separately for nonprecipitating clouds (class 1), precipitating clouds sensed from underneath the rain (class 2) and sensed from outside the rain (class 3). The quality criterion reduces the database by only 12%. A mean QI of 5.4 for class 2 indicates an overall good match between observations and simulations, but the large tail with values even above 15 indicates also that cases like the period from 04:06 to 04:36 UTC in Figure 6 are rather frequent. Although  $\text{QI} < 20$  indicates already a good match, the existence of retrievals with QI larger than 20 gives a clue on the limitations of this retrieval scheme. Sources of mismatching, which are not being taken into account in the forward model, are for instance the presence of a melting layer or nonuniform beam filling as it was shown by Battaglia *et al.* [2011].

It is important, however, to note that poor retrieval performance (large QI) like the period 04:09 to 04:15 UTC in Figure 7 could also be explained by a  $\sim -7^\circ$  antenna misalignment of the 10.7 GHz channels relative to the others, a shortcoming already noted by Battaglia *et al.* [2009a]. The current retrieval scheme takes this misalignment into account to some degree, by including in the database simulations of this proper misalignment [Battaglia *et al.*, 2009b, section 5].

[54] The IWV shows clearly a bimodal distribution for the three classes, with the peculiarity that for pure cloud retrievals (class 1) the lowest peak is shifted approximately  $8 \text{ kg m}^{-2}$  below the corresponding first peak at class 2. Since the pure cloud observations were selected either before or after the rain periods, this shift can be associated with an increase on water vapor yielded by rain events. The PDFs for CLWP and RLWP are heavily skewed, as expected, with CLWP holding a more populated tail than its rainy counterpart, especially for class 2, with an accumulation around  $1.3 \text{ kg m}^{-2}$ . On the other hand the cloud distribution for class 3 depicts fewer observations with low CLWP values, which can be due to the slant observational geometry since when dealing with finite cloud structure, the radiometer is likely to sense a larger cloud volume from a

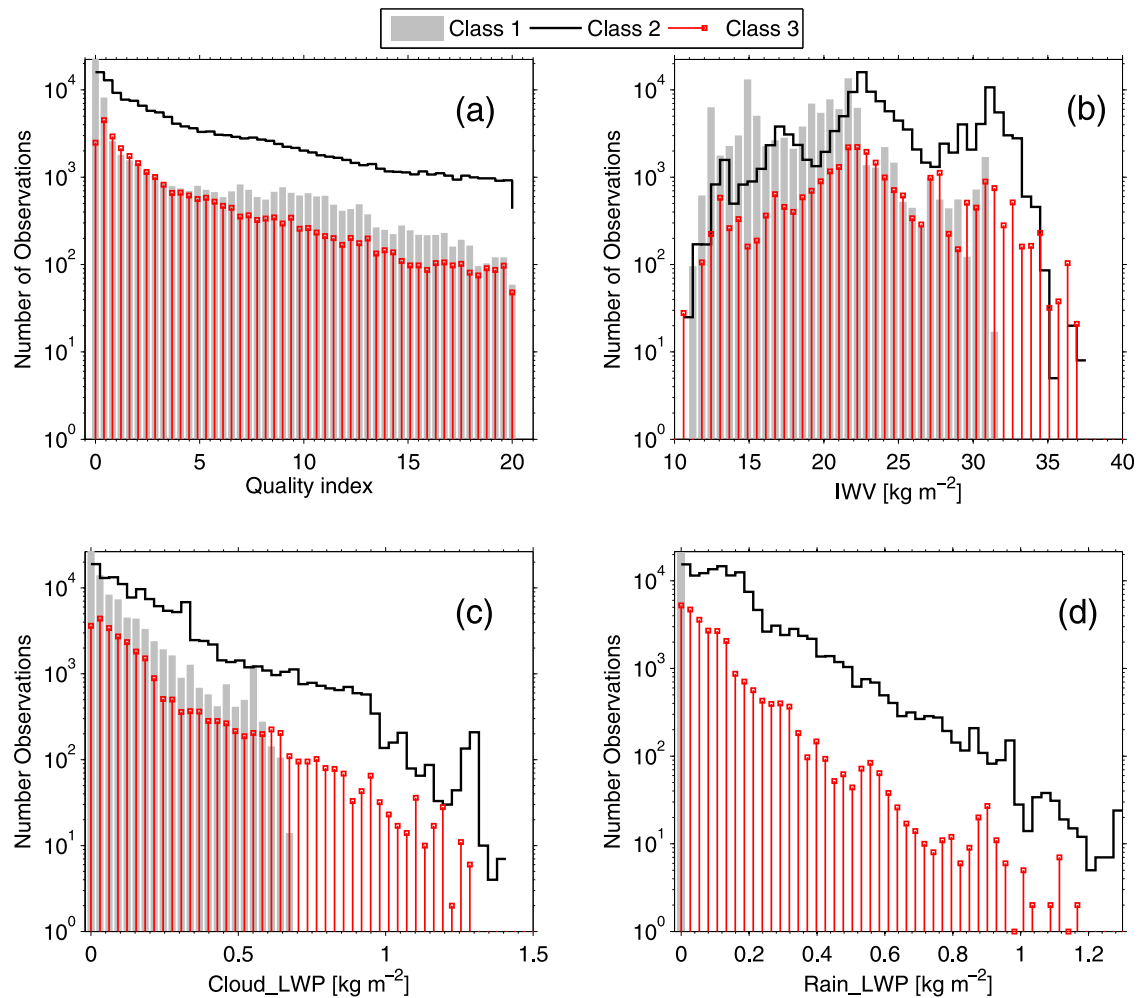


**Figure 9.** Histograms of (a) QI and retrieved (b) IWV, (c) CLWP, and (d) RLWP from 23 August to 12 November 2008. Statistics for pure cloud (class 1, gray area), radiometer inside the rain cell (class 2, solid black line), and radiometer outside the rain cell (class 3, red lines) are presented separately, as described in the text.

certain distance (class 3) than from underneath the cloud (class 2). The PDF of RLWP shows a more monotonically decreasing distribution with values ranging even till  $1.3 \text{ kg m}^{-2}$  for class 2, but only around  $1.0 \text{ kg m}^{-2}$  for the class 3.

[55] Table 2 summarizes the mean of the Bayesian standard deviation for the retrieved parameters of the three classes shown in Figure 9. The mean RMSE for cloud LWP is  $43 \text{ g m}^{-2}$  for rain-free cases; the accuracy is degraded to  $144.5 \text{ g m}^{-2}$  when cloud and rain LWP are retrieved simultaneously. It is observed that the RMSE presents a decrease of approximately 10% from class 2 to class 3 for both cloud and rain LWP, corroborated also by a reduction in QI. The RMSE for IWV increases from class 1 to class 3 only in the order of 20%.

[56] From Figure 7 and from the whole analyzed period it is observed that during rainy periods, the CLWP is retrieved with lower accuracy compared with its rain counterpart. The retrieved cloud RMSE by ADMIRARI are, however, smaller than the uncertainties values quoted by *Matrosov* [2009a, Figure 14] as typical for stratiform rain systems retrieved from a dual-frequency radar approach (i.e., cloud LWP

uncertainties ranging from  $\sim 100$  to  $\sim 600 \text{ g m}^{-2}$  for rain rates in the interval from 1 to  $10 \text{ mm h}^{-1}$ , respectively).

### 4.3. Discussion on Cloud-Rain Partition

[57] The cloud water–rainwater partition obtained by ADMIRARI is presented in Figure 10 (renormalized to vertical column) for precipitating clouds (class 2 and class 3 merged together). A large range of CLWP for low rain

**Table 2.** Mean of the Standard Deviation for the Retrieved Variables According to Three Classifications: (1) Nonprecipitating Clouds, (2) Radiometer Inside the Rain Cloud, and (3) Radiometer Outside the Rain Cloud

RMSE	Class 1	Class 2	Class 3
IWV ( $\text{kg m}^{-2}$ )	1.31	1.54	1.58
CLWP ( $\text{g m}^{-2}$ )	43.9	144.5	132.4
RLWP ( $\text{g m}^{-2}$ )	–	52.1	46.5
	Class 1	Class 2	Class 3
Mean quality index	2.5	5.4	3.9
Number of observations	78393	153400	28768

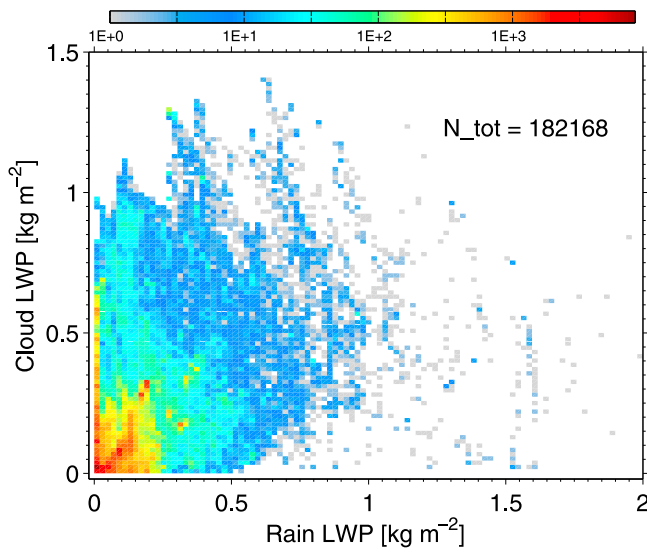


**Figure 10.** Retrieved partition for cloud and rain LWP during the whole observation period (class 2). The color bar indicates the number of observations in logarithmic scale.

contents is observed, with CLWP ranging from 0 to  $\sim 1 \text{ kg m}^{-2}$  while the RLWP stays  $< 0.06 \text{ kg m}^{-2}$  (every pixel represents a bin of  $\sim 0.02 \text{ kg m}^{-2}$ ), which can be attributed to observations corresponding to start and stop of precipitation as well as observation from outside the rain cell (class 3) since the slant radiometer FOV favors the sensing of the higher part of the precipitating cloud and catching only a small part of the rain component. In addition it sees a clear tendency on the cloud versus rain distribution to follow the 2:1 line until approximately  $0.4 \text{ kg m}^{-2}$  for either cloud and rain LWP, then the distribution spreads out with CLWP reaching as high as  $1.4 \text{ kg m}^{-2}$ , but that feature is not equally followed by the RLWP.

[58] The CLWP seems to level off at very high rainwater contents. No cloud LWP above  $1 \text{ kg m}^{-2}$  is observed with rain counterparts less than  $0.10 \text{ kg m}^{-2}$ . On the contrary it is feasible to find tens of observations with very large RLWP ( $> 1.5 \text{ kg m}^{-2}$ ) but low CLWP ( $< 0.2 \text{ kg m}^{-2}$ ) counterparts.

[59] Figure 10 provides a first overview of the statistics of cloud water versus rainwater for precipitating clouds attainable by a ground-based instrument, a product potentially extremely useful in the physical validation of passive microwave satellite rainfall retrievals, which inherently assume a cloud-rain partitioning. Different algorithms attributes different weights to the cloud and rain component and this is the cause of large discrepancies in the different precipitation product. For instance, *Hilburn and Wentz* [2008] compared the unified microwave ocean retrieval algorithm (UMORA) results with the cloud water–rainwater relationship obtained from the Goddard profiling algorithm (GPROF) on a pixel-to-pixel basis [*Kummerow et al.*, 2001, Figure A1]. The squared correlation coefficient between UMORA and GPROF for total liquid water is  $R^2 = 0.62$ , and for surface rain rate it is 0.56. GPROF attributes more water to precipitation and less to cloud water compared to UMORA. Typically, GPROF partitions  $0.5\text{--}1.0 \text{ kg m}^{-2}$  less cloud water for a given precipitation water than UMORA.

[60] It is obvious that our retrieved data set corresponds to ground-based observations for a specific location and a limited spell (representative of a midlatitude autumn precipitation) with high temporal and spatial resolution, while satellite products are related to vastly different sensed volumes and are applicable to the global scale over ocean. Despite these preliminary remarks, it is here interesting to briefly discuss how to establish a paradigm in ground validation field campaigns for validating the physical assumptions underpinning satellite retrievals.

[61] *Hilburn and Wentz* [2008] reported satellite derived relationships between columnar cloud water and rainwater over oceans for tropical observation relying on UMORA. On the basis of the work by *Wentz and Spencer* [1998] on northeast Pacific extratropical cyclones the following assumptions are made: (1) Rain is initiated at  $\text{CLWP} = 0.180 \text{ kg m}^{-2}$ . (2) CLWP increases with RLWP. (3) The cloud versus rain relationship levels off at high RLWP, with CLWP reaching a maximum value between 1 and  $2 \text{ kg m}^{-2}$ . The following are our respective findings:

[62] 1. For the EUCAARI ADMIRARI data set, clouds can support a CLWP (renormalized to vertical observations) larger than  $0.55 \text{ kg m}^{-2}$  before a rain components develops (see Figure 9c, class 1). Our findings are in line with other ground-based microwave observations like those documented by *Karstens et al.* [1994] who deduced a threshold CLWP of about  $0.5 \text{ kg m}^{-2}$  over the North Sea or those reported by *Crewell et al.* [2004] over the same CESAR site. On the other hand rain is observed even at cloud LWPs below  $0.55 \text{ kg m}^{-2}$  (see, e.g., Figure 7, period from 06:39 to 06:51 UTC). A large population of the cloud versus rain distribution depicts a tend to follow the 2:1 line, interestingly similar observation is reported by *Lebsock et al.* [2011] for precipitating shallow marine clouds with occurrence of rain at very low cloud water paths even below  $200 \text{ g m}^{-2}$ .

[63] 2. ADMIRARI results do not seem to favor a well defined functional relationship between CLWP and RLWP as obtained by UMORA; they resemble more the GPROF distribution. The GPROF cloud-rain partitioning displays a branch of cloud LWP with maximum values of  $\sim 1.0 \text{ kg m}^{-2}$  starting at very low rain contents e.g.,  $\text{RLWP} < 0.3 \text{ kg m}^{-2}$ , which agrees quite well with the ADMIRARI results; here maximum cloud values of  $\sim 1.1 \text{ kg m}^{-2}$  are observed for RLWP below  $0.3 \text{ kg m}^{-2}$ .

[64] 3. The maximum CLWP for a given RLWP tends to level off at  $\sim 1.4 \text{ kg m}^{-2}$  while the rain LWP still increases.

[65] More conclusive assessments of the satellite inherent assumptions could be drawn only by adopting long-term field campaign strategies involving ADMIRARI-like measurements and targeting specific precipitation regimes. The effect of the mismatch between space and ground-based sensed volumes could be reduced by properly temporally averaging the ground-based retrieved products.

## 5. Summary and Conclusions

[66] ADMIRARI is a multifrequency (10.7–21.0–36.5 GHz) scanning radiometer measuring horizontally and vertically polarized brightness temperatures. Its polarization and multifrequency capabilities have been envisaged to enable the partitioning of cloud and rain along the line of sight. As a test bed, ADMIRARI performed measurements

at 30° elevation at the CESAR observatory in Cabauw, the Netherlands, between 23 August and 12 November 2008. The ADMIRARI measurements are complemented by MRR reflectivity profiles along the same line of sight. A total of about 72 h of quality-controlled observations of precipitating clouds are collected.

[67] A simulation-based retrieval sensitivity study confirms the suitability of retrieving simultaneously integrated cloud water, rain water, and water vapor from the ADMIRARI measurements by a Bayesian inversion algorithm. The additional constrain of the rain distribution within the line of sight provided by the colocated MRR improves the accuracy of the retrieval by confining the number of profiles entering the Bayesian average to structurally comparable profiles. It has been found that for cases with very low water content the ADMIRARI approach, to distinguish cloud and rain from the total water content, can produce large uncertainties. The incorporation of the radar reflectivity profiles into the retrieval technique has been evaluated in the sensitivity study, showing large improvement in the retrieval uncertainties, specially for the cases with low rain-cloud LWP. This approach paves the way toward a synergistic retrieval technique combining active and passive measurements, but a full incorporation of the MRR reflectivity profiles needs more detailed studies mainly because of FOV mismatching and MRR calibration issues, which is the reason that only geometrical constraints have been included in the present work. We strongly recommend the exploitation of radars with radiometric mode for the simultaneous retrieval of cloud and rain contents. Studies in this direction with the new multifrequency scanning ARM radars are now in progress. When deployed colocated with such instruments the ADMIRARI retrievals could be validated by independent products. ADMIRARI is currently taking part in the Global Precipitation Measurements (GPM) Ground Validation Programme (<http://gpm.gsfc.nasa.gov/groundvalidation.html>), which, given the abundance of ancillary measurements, will represent a paramount opportunity to tackle the validation issue for the ADMIRARI products.

[68] The forward modeling used to construct the retrieval database is capable of reproducing the observed brightness temperatures and polarization differences within the model and instrument errors. Only 12% of the data are dismissed because of high residuals. This indicates that there is still room for improving the forward model, e.g., by accounting for nonuniform beam filling effects, by including full horizontal spatial variability of the cloud structure and by considering a realistic melting layer. In order to address the latter issue, ADMIRARI has been deployed from September 2010 to January 2011 in Helsinki as part of the Light Precipitation Validation experiment. The observation of precipitating systems with very low freezing levels is ideal to isolate the multifrequency microwave signatures of melting particles and to identify appropriate electromagnetic and microphysical models [Szyrmer and Zawadzki, 1999] to be incorporated in the forward model. In addition, the construction of more representative a priori data set will be pursued by mimicking the work of Kummerow *et al.* [2011] for the passive microwave retrievals over ocean using the operational TRMM precipitation radar. That could allow us to reduce the uncertainties in the assumptions about the a

priori introduced by utilizing climatological CRM simulations only.

[69] When applied to the whole measurement data sets, rain, cloud, and water vapor integrated parameters are retrieved with average errors of about 50 g m<sup>-2</sup>, 150 g m<sup>-2</sup>, and 1.6 kg m<sup>-2</sup>, respectively. Clearly, the main uncertainties lay on the cloud component with the cloud RMSE significantly higher than typical values expected from passive microwave retrievals for nonprecipitating clouds (~20–40 g m<sup>-2</sup> [Loehnert and Crewell, 2003]). In presence of low LWP the partitioning between cloud and rain is prone to large errors. Below 450 g m<sup>-2</sup> only the total LWP can be retrieved properly with RMSE around 40 g m<sup>-2</sup>. This mirrors the obvious fact that small rain contents are associated with almost spherical raindrops which do not produce polarized signals and dwarf the ADMIRARI potential. When the radar reflectivity information is utilized the RMSE for total LWP can be reduced to even 13 g m<sup>-2</sup>.

[70] The results of our work represent the first continuous long-term retrieval of integral parameters from precipitating clouds derived by ground-based microwave observations. While these results are representative of the specific climatological regime and observational configuration, they certainly reveal the potential of ground-based passive microwave polarimetric observations to constrain the microphysical assumptions on the cloud-rain partition underpinning spaceborne microwave-based retrievals and therefore to reduce their LWP errors [O'Dell *et al.*, 2008]. The GPM ground validation experiments provide the best test bed to extend ADMIRARI observations to tropical and high-latitude precipitation. As such, ADMIRARI will contribute to a deeper understanding of precipitating cloud parameters and offer unprecedented information for cloud modeling and for the validation of GPM space-based rain retrieval algorithms. The present work set certainly a milestone in such research avenue.

## Appendix A: Rain LWP Retrieval From Pure MRR Data

[71] Since the MRR was sensing exactly at the same elevation angle as ADMIRARI, a pure MRR-based RLWP estimation can be treated as an independent retrieval. Although the MRR reflectivity data is susceptible to miscalibration and attenuation, rain LWP can be estimated from the equivalent reflectivity per unit volume  $Z$  (in mm<sup>6</sup> m<sup>-3</sup>),

$$Z = \frac{\lambda^4}{\pi^5 |\kappa|^2} \int_0^\infty \sigma_b^{MIE} N(D) dD \quad (\text{A1})$$

where  $\sigma_b^{MIE}$  is the backscattering cross section computed according to MIE theory,  $\lambda$  is the MRR wavelength (12.4 mm),  $\kappa = \frac{m^2 - 1}{m^2 + 2}$  is the dielectric factor with  $m$  being the complex index of refraction of the hydrometeor, and  $N(D)$  is the inverse exponential DSD (equation (10)) modulated by its slope parameter  $\Lambda$  which depends on the liquid water content following:

$$\Lambda = \left( \frac{N_0 \pi \rho_w}{\text{LWC}} \right)^{\frac{1}{4}} \quad (\text{A2})$$

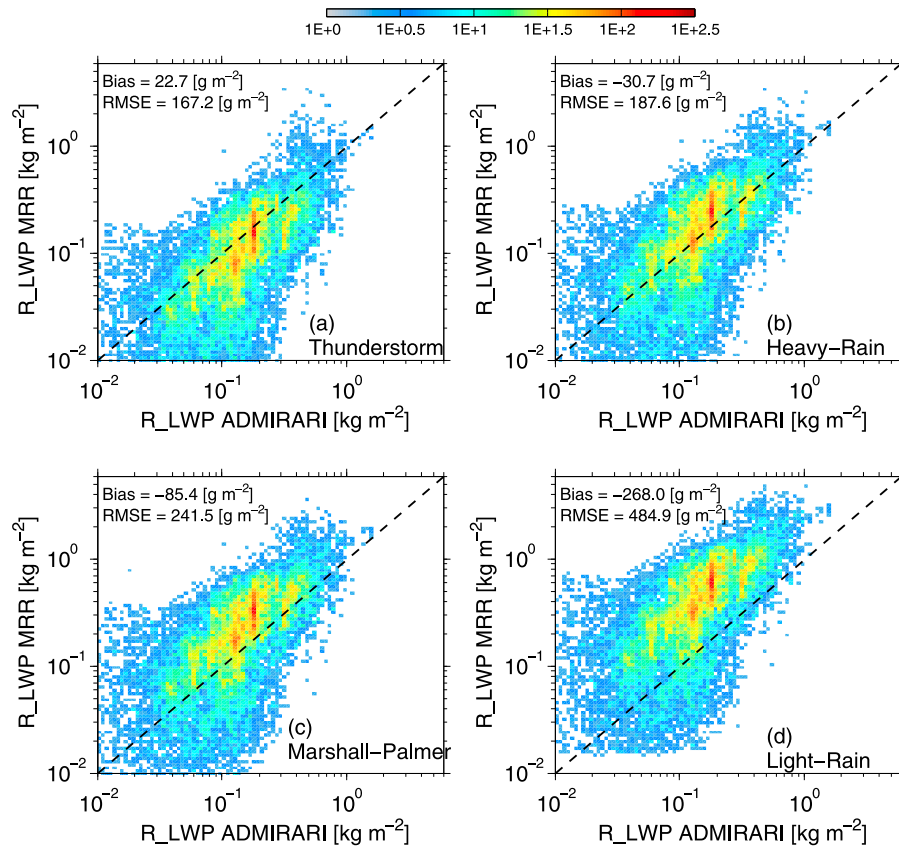


**Figure A1.** Distribution of rain LWP retrieved by ADMIRARI versus the estimation from MRR by using equation (A3) for  $N_0 = 1.4, 4.0, 8.0,$  and  $32.0 \times 10^3 \text{ m}^{-3} \text{ mm}^{-1}$  at (a) thunderstorm, (b) heavy rain, (c) Marshall-Palmer, and (d) light rain. The black dashed line indicates the 1:1 relation, and the color bar indicates the number of repetitions.

with the rain liquid water content (LWC) in  $\text{g m}^{-3}$  and  $\rho_w$  is the water density in  $\text{g m}^{-3}$  and  $N_0$  is the exponential DSD intercept parameter which takes the four values of 1.4, 4.0, 8.0, and  $32.0 \times 10^3 \text{ m}^{-3} \text{ mm}^{-1}$  for thunderstorm, heavy rain, Marshall-Palmer, and light rain, respectively. The radar rain liquid water path is obtained by mapping back the reflectivity obtained after combining equations (A2) and (A1), given a certain LWC, by

$$\text{RLWP}_{(N_0)} = \int \text{LWC}_{(s, N_0)} ds, \quad (\text{A3})$$

with the integral evaluated over the slant MRR range  $s$ . The MRR RLWP is shown against its ADMIRARI counterpart in Figure A1 for the four  $N_0$  values.

[72] Figure A1 depicts a large dispersion of RLWP when the ADMIRARI and the independent MRR retrievals are compared pixel to pixel. A general feature is that the MRR tends to accumulate large range of retrievals for certain ADMIRARI values (see, for instance, the large populated vertical strips in Figure A1). For the thunderstorm or heavy rain cases, the distribution maxima follow the one to one line, with the lowest bias and a RMSE of  $167.2 \text{ g m}^{-2}$  (Figure A1a). The opposite is obtained for the light rain case (Figure A1d) showing a large overestimation in the MRR retrievals, with the ADMIRARI results practically completely overestimated for RLWP above  $\sim 0.4 \text{ kg m}^{-2}$ , with

MRR counterpart reaching values as high as  $3 \text{ kg m}^{-2}$ . The Marshall and Palmer DSD assumption already shows a slight tendency to overestimate the rainwater path respect to the ADMIRARI. In summary, Figure A1 indicates that in the pure MRR-based retrieval, it is necessary to favor large DSDs for practically all the retrieval cases in order to reproduce the ADMIRARI Bayesian retrievals. That conclusion is corroborated by the fact that from all rain events analyzed in this work, more than 80% have convective nature.

[73] **Acknowledgments.** The ADMIRARI project was funded by the Deutsche Forschungsgemeinschaft (DFG) under grant BA 3485/1-1. The authors would like to thank the staff of the CESAR observatory for hosting ADMIRARI and for providing ancillary data during the EUCAARI field campaign. A. Battaglia's travel costs were covered by the NCEO-EO Mission Support.

## References

- Battaglia, A., and C. Simmer (2007), Explaining the polarization signal from rain dichroic media, *J. Quant. Spectrosc. Radiat. Transfer*, 105(1), 84–101.
- Battaglia, A., H. Czekala, and C. Simmer (2006), Three dimensional effects in polarization signatures as observed from precipitating clouds by low frequency microwave radiometer, *Atmos. Chem. Phys.*, 6, 4383–4394.
- Battaglia, A., C. Davis, C. Emde, and C. Simmer (2007), Microwave radiative transfer intercomparison study for 3-D dichroic media, *J. Quant. Spectrosc. Radiat. Transfer*, 105(1), 55–67.

- Battaglia, A., P. Saavedra, C. Simmer, and T. Rose (2009a), Rain observation by a multifrequency dual-polarized radiometer, *IEEE Geosci. Remote Sens. Lett.*, *6*, 354–358, doi:10.1109/LGRS.2009.2013484.
- Battaglia, A., P. Saavedra, T. Rose, and C. Simmer (2009b), Characterization of precipitating clouds by ground-based measurements with the triple-frequency polarized microwave radiometer ADMIRARI, *J. Appl. Meteorol.*, *49*(3), 394–414.
- Battaglia, A., P. Saavedra, C. A. Morales, and C. Simmer (2011), Understanding three-dimensional effects in polarized observations with the ground-based ADMIRARI radiometer during the CHUVA campaign, *J. Geophys. Res.*, *116*, D09204, doi:10.1029/2010JD015335.
- Bennartz, R., P. Watts, J. F. Meirink, and R. Roebeling (2010), Rainwater path in warm clouds derived from combined visible/near-infrared and microwave satellite observations, *J. Geophys. Res.*, *115*, D19120, doi:10.1029/2009JD013679.
- Crewell, S., and U. Loehnert (2003), Accuracy of cloud liquid water path from ground-based microwave radiometry: 2. Sensor accuracy and synergy, *Radio Sci.*, *38*(3), 8042, doi:10.1029/2002RS002634.
- Crewell, S., H. Czekala, U. Loehnert, C. Simmer, T. Rose, R. Zimmermann, and R. Zimmermann (2001), Microwave radiometer for cloud cartography: A 22-channel ground-based microwave radiometer for atmospheric research, *Radio Sci.*, *36*(4), 621–638.
- Crewell, S., et al. (2004), The BALTEX Bridge Campaign—An integrated approach for a better understanding of clouds, *Bull. Am. Meteorol. Soc.*, *85*(10), 1565–1584, doi:10.1175/BAMS-85-10-1565.
- Crewell, S., K. Ebell, U. Loehnert, and D. D. Turner (2009), Can liquid water profiles be retrieved from passive microwave zenith observations?, *Geophys. Res. Lett.*, *36*, L06803, doi:10.1029/2008GL036934.
- Czekala, H., and C. Simmer (1998), Microwave radiative transfer with non-spherical precipitating hydrometeors, *J. Quant. Spectrosc. Radiat. Transfer*, *60*(3), 365–374.
- Czekala, H., S. Crewell, C. Simmer, and A. Thiele (2001a), Discrimination of cloud and rain liquid water path by ground based polarized microwave radiometry, *Geophys. Res. Lett.*, *28*, 267–270.
- Czekala, H., S. Crewell, A. Hornbostel, A. Schroth, C. Simmer, and A. Thiele (2001b), Interpretation of polarization features in ground-based microwave observations as caused by horizontally aligned oblate raindrops, *J. Appl. Meteorol.*, *40*, 1918–1932.
- Gaussiat, N., R. J. Hogan, and J. Illingworth (2007), Accurate liquid water path retrieval from low-cost microwave radiometers using additional information from a lidar ceilometer and operational forecast models, *J. Atmos. Oceanic Technol.*, *24*, 1562–1575.
- Hilburn, K. A., and F. J. Wentz (2008), Intercalibrated passive microwave rain products from the unified microwave ocean retrieval algorithm (UMORA), *J. Appl. Meteorol.*, *47*, 778–794, doi:10.1175/2007JAMC1635.1.
- Evans, K. F., and G. L. Stephens (1991), A new polarized atmospheric radiative transfer model, *J. Quant. Spectrosc. Radiat. Transfer*, *46*, 413–423.
- Karstens, U., C. Simmer, and E. Ruprecht (1994), Remote sensing of cloud liquid water, *Meteorol. Atmos. Phys.*, *54*, 157–171.
- Kneifel, S., M. Maahn, G. Peters, and C. Simmer (2011), Observation of snowfall with a low-power FM-CW K-band radar micro rain radar, *Meteorol. Atmos. Phys.*, *113*, 75–87.
- Knupp, K. R., R. Ware, D. Cimini, F. Vandenbergh, J. Vivekanandan, E. Westwater, T. Coleman, and D. Phillips (2009), Ground-based passive microwave profiling during dynamic weather conditions, *J. Atmos. Oceanic Technol.*, *26*, 1057–1073.
- Kummerow, C., W. S. Olson, and L. Giglio (1996), A simplified scheme for obtaining precipitation and vertical hydrometeor profiles from passive microwave sensor, *IEEE Trans. Geosci. Remote Sens.*, *34*(5), 1213–1232.
- Kummerow, C., Y. Hong, W. S. Olson, S. Yang, R. F. Adler, J. McCollum, R. Ferraro, G. Petty, D.-B. Shin, and T. T. Wilheit (2001), The evolution of the Goddard profiling algorithm (GPROF) for rainfall estimation from passive microwave sensors, *J. Appl. Meteorol.*, *40*, 1801–1820.
- Kummerow, C. D., S. Ringerud, J. Crook, D. Randel, and W. Berg (2011), An observationally generated a priori database for microwave rainfall retrievals, *J. Atmos. Oceanic Technol.*, *28*, 113–130, doi:10.1175/2010JTECHA1468.1.
- Lebsack, M. D., T. L'Ecuyer, and G. L. Stephens (2011), Detecting the ratio of rain and cloud water in low-latitude shallow marine clouds, *J. Appl. Meteorol. Climatol.*, *50*, 419–432, doi:10.1175/2010JAMC2494.1.
- Loehnert, U., and S. Crewell (2003), Accuracy of cloud liquid water path from ground-based microwave radiometry: 1. Dependency on cloud model statistics, *Radio Sci.*, *38*(3), 8041, doi:10.1029/2002RS002654.
- Loehnert, U., S. Kneifel, A. Battaglia, M. Hagen, L. Hirsch, and S. Crewell (2011), A multi-sensor approach towards a better understanding of snowfall microphysics: The TOSCA project, *Bull. Am. Meteorol. Soc.*, *92*, 613–628, doi:10.1175/2010BAMS2909.1.
- Maetzler, C., and J. Morland (2008), Advances in surface-based radiometry of atmospheric water, *IAP Res. Rep. 2008-02-MW*, Inst. Angew. Phys., Univ. Bern, Bern, Switzerland.
- Marzano, F. S., A. Mugnai, G. Panegrossi, N. Pierdicca, E. Smith, and J. Turk (1999), Bayesian estimation of precipitating cloud parameters from combined measurements of spaceborne microwave radiometer and radar, *IEEE Trans. Geosci. Remote Sens.*, *37*, 596–613.
- Marzano, F. S., D. Cimini, P. Ciotti, and R. Ware (2005a), Modeling and measurements of rainfall by ground-based multispectral microwave radiometry, *IEEE Trans. Geosci. Remote Sens.*, *43*, 1000–1011.
- Marzano, F. S., D. Cimini, and R. Ware (2005b), Monitoring of rainfall by ground-based passive microwave systems: Models, measurements and applications, *Adv. Geosci.*, *2*, 259–265.
- Matrosov, S. Y. (2009a), A method to estimate vertically integrated amounts of cloud ice and liquid and mean rain rate in stratiform precipitation from radar and auxiliary data, *J. Appl. Meteorol.*, *48*, 1398–1410, doi:10.1175/2009JAMC2196.1.
- Matrosov, S. Y. (2009b), Simultaneous estimates of cloud and rainfall parameters in the atmospheric vertical column above the Atmospheric Radiation Measurement Program southern Great Plains site, *J. Geophys. Res.*, *114*, D22201, doi:10.1029/2009JD012004.
- McFarlane, S. A., F. K. Evans, and A. S. Ackerman (2002), A Bayesian algorithm for the retrieval of liquid water cloud properties from microwave radiometer and millimeter radar data, *J. Geophys. Res.*, *107*(D15), 4271, doi:10.1029/2001JD000383.
- Meteorologische Messtechnik GmbH (2005), Micro rain radar physical models version 1.9.0, Elmshorn, Germany.
- O'Dell, C. W., F. Wentz, and R. Bennartz (2008), Cloud liquid water path from satellite-based passive microwave observations: A new climatology over the global ocean, *J. Clim.*, *1*(8), 1721–1739, doi:10.1175/2007JCLI1958.1.
- Rodgers, S. D. (2000b), *Inverse Methods for Atmospheric Sounding: Theory and Practice*, World Sci., Singapore.
- Rose, T., S. Crewell, U. Loehnert, and C. Simmer (2005), A network suitable microwave radiometer for operational monitoring of the cloudy atmosphere, *Atmos. Res.*, *75*, 183–200, doi:10.1016/j.atmosres.2004.12.2005.
- Salby, M. L. (1996), *Fundamentals of Atmospheric Physics, Int. Geophys. Ser.*, vol. 61, Academic, San Diego, Calif.
- Stephens, G. L., and P. J. Webster (1984), Cloud decoupling of the surface and planetary radiative budgets, *J. Atmos. Sci.*, *41*, 681–686.
- Szyrmer, W., and I. Zawadzki (1999), Modeling of the melting layer. Part I: Dynamics and microphysics, *J. Atmos. Sci.*, *56*, 3573–3592.
- Tao, W. K., and J. Simpson (1993), Goddard Cumulus Ensemble Model. Part I: Model description, *Terr. Atmos. Oceanic Sci.*, *4*(1), 35–72.
- Wentz, F. J., and R. W. Spencer (1998), SSM/I rain retrievals within a unified all-weather ocean algorithm, *J. Atmos. Sci.*, *55*, 1613–1627.

A. Battaglia, Department of Physics and Astronomy, University of Leicester, University Road, Leicester LE1 7RH, UK. (a.battaglia@le.ac.uk)  
 P. Saavedra and C. Simmer, Meteorological Institute, University of Bonn, Auf dem Hügel 20, D-53121 Bonn, Germany. (pablosaa@uni-bonn.de; csimmer@uni-bonn.de)